Master Thesis Physics

Track: Particle and Astroparticle Physics

Cosmics in the LHCb Outer Tracker

Roel Aaij

B–physics Department

Nikhef

University of Amsterdam

Supervisor: Thomas Bauer

January 2010

University of Amsterdam

NIKHEF

Abstract

The LHCb experiment at the Large Hadron Collider studies the decay of B mesons to test the description of CP violation in the Standard Model and to search for new physics. The decay $B_s \to \mu^+\mu^-$ has been identified as very promising in the search for new physics. An excellent invariant mass resolution is required to suppress backgrounds to this decay. This in turn requires a momentum resolution of $\mathrm{d}p/p = 0.4\%$.

The Outer Tracker is part of the LHCb tracking system and has been commissioned with cosmic muons. The noise in the Outer Tracker is shown to be less than 0.05%. To use drift time information in the reconstruction of cosmic tracks, the event time must be known. Four methods to obtain the event time are studied and compared. It is shown that the event time can be obtained with a resolution better than 2.6 ns. Using drift time information, tracks are reconstructed with a resolution of 344 µm.

Knowledge of the event time enables the calibration of electronic time offsets and the $r(t)$–relation. Application of obtained electronic time offsets improves the resolution of tracks to 334 µm, while calibration of the $r(t)$–relation is unsuccessful. A spatial resolution of 334 µm is sufficient to obtain the required momentum resolution.

Contents

Chapter 1

Introduction

Previous and current generations of particle accelerators and their experiments have provided a detailed understanding of physics at energies up to the TeV scale. The predictions of the Standard Model of particle physics have been tested and, so far, found to be in agreement with experimental results. Nevertheless, unanswered questions remain. Neither is the Standard Model able to explain the nature of cold dark matter, nor does it give rise to the observed asymmetry between matter and antimatter in the universe.

Sakharov showed that CP violation is one of the conditions for the presence of such an asymmetry in the universe [1]. In the Standard Model of particle physics, the weak interaction is the sole origin of CP violation, which in turn is a result of the single complex parameter of the CKM matrix [2]. All measurements of the elements of the CKM matrix allow for a unitarian CKM matrix within errors, as predicted by the Standard Model. The further constraint of the CKM matrix is one of the main goals of the LHCb experiment at the Large Hadron Collider at Cern [3].

The other purpose of the LHCb experiment is to search for physics beyond the Standard Model by measuring the branching ratio of several rare decays of B mesons. The measurement of the branching ratio of the decay $B_s \rightarrow \mu^+\mu^-$ is considered especially promising. It is predicted to be $3.35 \pm 0.32 \times 10^{-9}$ in the Standard Model, while various models for new physics predict it to be up to an order of magnitude higher. An excellent invariant mass resolution is needed to reduce the background for this decay, which in turn requires the LHCb tracking system to reconstruct particle tracks with a good momentum resolution. Chapter 2 discusses some of the physics motivating the LHCb experiment in more detail.

Chapter 3 focuses on the LHCb detector and its Outer Tracker in particular. The Outer Tracker is part of the LHCb tracking system and contributes to the finding and reconstruction of particle tracks and the reduction of the number of wrongly reconstructed tracks. During my research project I analysed cosmic muon data as a part of the Outer Tracker commissioning effort. The purpose of the analysis is to determine how well tracks from cosmic muons can be reconstructed and which information can be obtained from these tracks. The data was recorded in November and December of 2008 and consists of approximately two hundred thousand events. Approximately ten percent of the events contains a track in the Outer Tracker.

Chapter 4 describes the properties of cosmic muons underground and how their tracks are reconstructed. Chapter 5 contains the results of the reconstruction of tracks from cosmic muons in the Outer Tracker. Particular attention is paid to the determination of the time of arrival of a muon with respect to the clock which controls the readout of the detector. The results of the calibration of the Outer Tracker are also presented.

The LHCb event display software is discussed in the last chapter of this thesis, chapter 6. The general structure of the software is described and a method to visualise Outer Tracker drift times is presented together with displays of events from data taken when particles were injected into the LHC from the Super Proton Synchrotron.

Chapter 2

Physics

The search for physics beyond the Standard Model requires continuing tests of the Standard Model with increasing accuracy. One area which has been extensively tested, is the area of the weak interaction. One of the defining properties of the weak interaction is that it enables transitions between quarks of up–type and down–type flavours and vice-versa through the exchange of charged W bosons.

2.1 The CKM Matrix

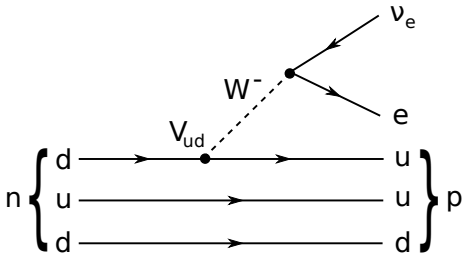

Figure 2.1: The Feynman diagram that describes the first order contribution to the beta decay of the neutron.

Transitions between up-type and down-type quarks are possible since the weak interaction eigenstates are a superposition of the quark mass eigenstates. The weak interaction eigenstates can be obtained from their mass eigenstates by multiplication with the CKM-matrix:

$$\begin{pmatrix} d' \\ s' \\ b' \end{pmatrix} = \begin{pmatrix} V_{ud} & V_{us} & V_{ub} \\ V_{cd} & V_{cs} & V_{cb} \\ V_{td} & V_{ts} & V_{tb} \end{pmatrix} \begin{pmatrix} d \\ s \\ b \end{pmatrix} . \tag{2.1}$$

A Feynman diagram which contains the first order contribution to the transition of an up quark to a down quark is shown in figure 2.1.

The CKM matrix was in part introduced by Cabibbo in 1963 [4]; it then contained only the u, d and s quarks. It was later extended to include the c–quark by Glashow, Iliopoulos and Maiani [5], in order to explain the extremely small decay rate of $K^0 \to \mu^+\mu^-$, which is about nine orders of magnitude smaller than the decay rate of the equivalent decay $K^+ \to \mu^+\nu$. In

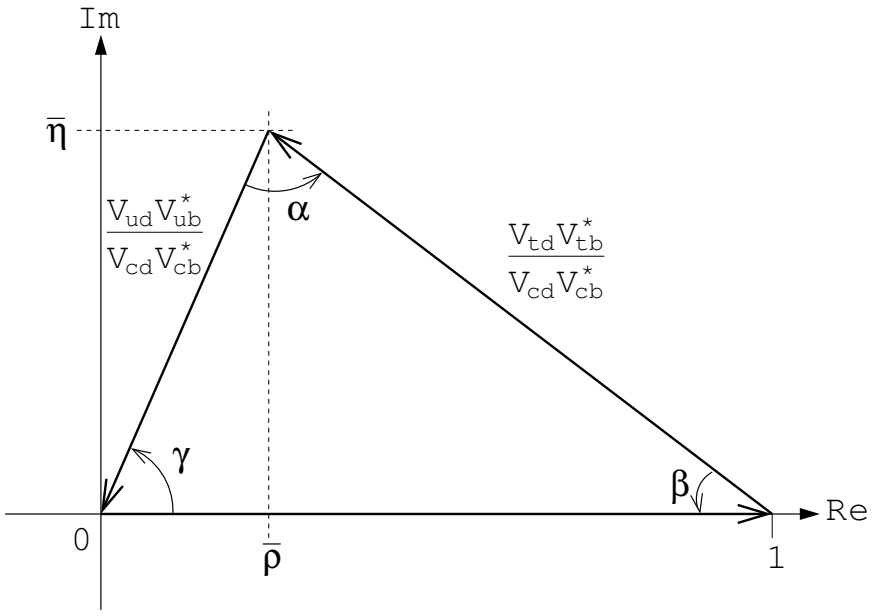

Figure 2.2: The unitarity triangle which visualises equation 2.3.

the so–called GIM mechanism,

$$\begin{pmatrix} d' \\ s' \end{pmatrix} = \begin{pmatrix} \cos\theta & \sin\theta \\ -\sin\theta & \cos\theta \end{pmatrix} \begin{pmatrix} d \\ s \end{pmatrix}, \tag{2.2}$$

where θ is the Cabibbo angle. The unitarity of this mixing matrix causes all flavour changing neutral currents to cancel, and the small branching ratio of $K^0 \to \mu^+\mu^-$ becomes a consequence of the cancellation of Feynman diagrams involving u and c quarks; in 1970, GIM thus postulated a fourth quark. Even before this fourth quark had been discovered, Kobayashi and Maskawa realised that a postulating the existence of a third generation of quarks presented a possibility to include CP violation in the Standard Model. CP violation had been discovered in the decay of neutral kaons in 1964 [6]. Kobayashi and Maskawa proposed to extend the CKM matrix to its current form [2].

In general, a $n \times n$ complex matrix consist of $2n^2$ independent parameters. Unitarity of a matrix results in n^2 constraints, leaving n^2 free parameters. As the CKM matrix deals with six quarks, six arbitrary phases can be absorbed by redefining the quark fields, keeping one overall phase. This leaves four parameters which need to be determined experimentally: three rotation angles and one complex phase. This complex phase is the source of CP violation in the Standard Model of weak interactions [2].

The unitarity of the CKM matrix implies nine constraining relations between the matrix elements. Three of these constraints can be formulated as $\sum_j |V_{ij}|^2 = 1$ for each generation i. This states that the number of quarks is conserved in the weak interaction and that the sum of all couplings of an up-type quark to each of the down-type quarks is identical for each of the generations. The other six relations are orthogonality conditions and can be written as $\sum_k V_{ik}V_{jk}^* = 0 (i \neq j)$; three relations define the orthogonality of the rows and three the orthogonality of the columns of the matrix. Each of these relations can be represented by a triangle in the complex plane [7]. The relation which has been most strongly constrained by experimental results is:

$$V_{ud}V_{ub}^* + V_{cd}V_{cb}^* + V_{td}V_{tb}^* = 0; \tag{2.3}$$

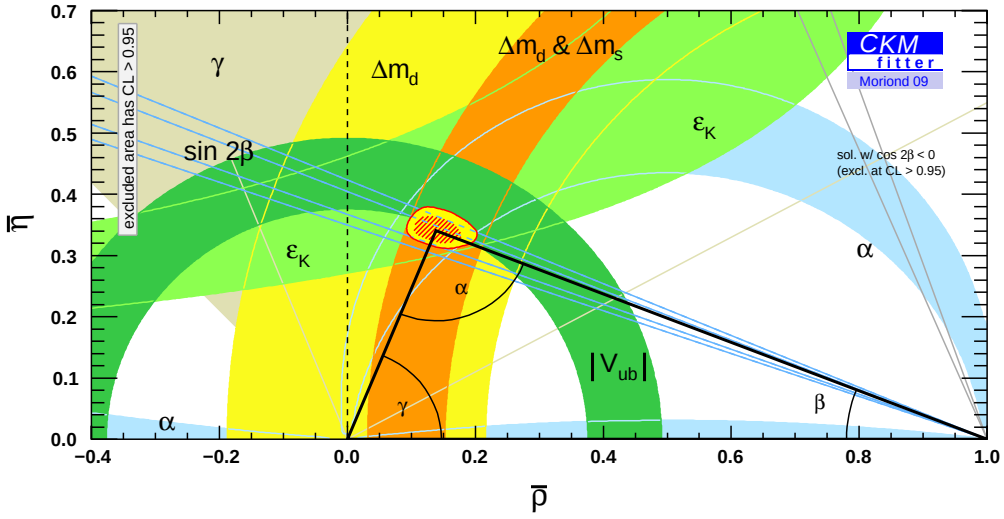

Figure 2.3: Current status of constraints on the unitarity triangle of equation 2.3 [14].

Dividing all terms in equation 2.3 by $V_{cd}V_{cb}^*$ results in the unitarity triangle shown in figure 2.2.

The description of CP violation in the Standard Model can be tested by determining all elements of the CKM matrix. Measuring the angles and lengths of the sides of all possible unitarity triangles over-constrains the CKM matrix, which offers the possibility of finding evidence of new physics if any constraints are observed to be inconsistent. The existing measurements relating to the angles α, β and γ, have predominantly been made by the *BABAR*, Belle CDF and D0 experiments and are shown as contour constraints on the angles in figure 2.3. These measurements include direct measurements of the CP phases α, β and γ by the B factory experiments, *BABAR*and Belle, such as the measurement of $\sin 2\beta$ in the $B^0 \to J/\psi\, K_S^0$ channel [8, 9]. The circle contours around $(1, 0)$ originate from measurements of the oscillation frequencies of the B^0 [10] and B_s [11, 12]. Circle contours around $(0, 0)$ represent $|V_{ub}|$ [10], and the hyperbola comes from ϵ in the kaon system [13].

As can be seen from figure 2.3, all measurements are consistent with Standard Model predictions; it can also be seen that if the accuracy of the constraints increases, they may no longer be consistent. This is particularly true for the angle γ, which is currently know to be $77 \pm 30°$ [15]. A better determination of γ might yield a result which is incompatible with the triangle shown in figure 2.3. The LHCb experiment is designed to measure the decay of B mesons with two primary goals: to improve the constraints on relevant CKM matrix elements and to search for new physics in rare decays of B mesons. Due to the high luminosity available at the LHC, LHCb will be able to determine γ in a model–independent way [16].

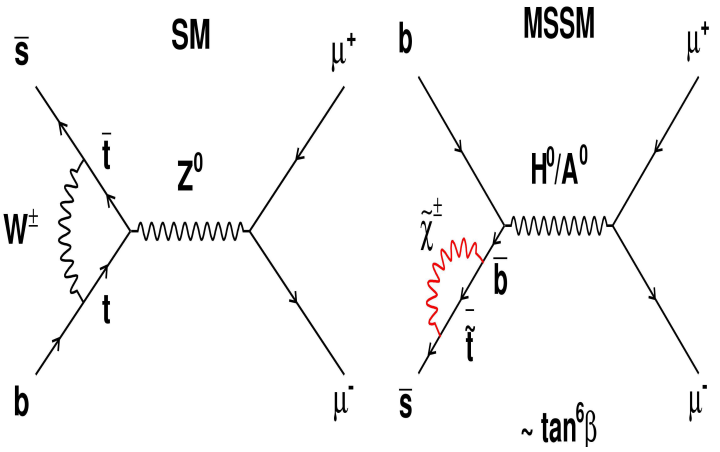

Figure 2.4: Feynman diagrams contributing to the decay $B_s \to \mu^+\mu^-$ in the Standard Model (left) and in the Minimally Super Symmetric extension of the Standard Model [21].

2.2 The Decay $B_s \to \mu^+\mu^-$

The decay $B_s \to \mu^+\mu^-$ has been identified as an interesting potential constraint in the parameter space of models for physics beyond the Standard Model [17]. It is heavily suppressed in the Standard Model by the GIM mechanism [5]; the current prediction has been computed to be $\mathrm{BR}(B_s \to \mu^+\mu^-) = (3.35 \pm 0.32) \times 10^{-9}$ [18]. the CDF and D0 experiments at the Tevatron collider at Fermilab have determined an upper limit on the branching ratio of $\mathrm{BR}(B_s \to \mu^+\mu^-) < 5.8 \times 10^{-8}$ at 95% confidence level [19].

Figure 2.4a shows the Feynman diagram that describes the highest order contribution to the decay in the Standard Model. Two diagrams similar to figure 2.4a exist, which contain a pair of $u, \overline{u}$ or $c, \overline{c}$ quarks instead of a pair of $t, \bar{t}$ quarks. The GIM mechanism causes these three diagrams to destructively interfere, thereby suppressing the branching ratio. Figure 2.4b shows an example of a "Higgs Penguin" diagram that would modify the Standard Model prediction and depends on $\tan^6\beta$. The diagram contains a number of particles which are predicted by the Minimally Supersymmetric extension of the Standard Model (MSSM), such as the stop quark, $\tilde{t}$, the CP–odd Higgs boson, A^0 and the chargino, $\tilde{\chi}^{\pm}$. The branching ratio of $B_s \to \mu^+\mu^-$ is known to be proportional to the sixth power of the ratio of Higgs vacuum expected values, $\tan\beta$ [20] and any improvement on its limit is of particular importance to models with large $\tan\beta$.

Given the low branching ratio of the decay $B_s \to \mu^+\mu^-$, the real challenge does not lie in the reconstruction of the signal, but in the reduction of backgrounds. Since there are only two particles in the final state, a good invariant mass resolution is of crucial importance to reduce the search window, the level of combinatorial background and the number of misidentified two–body decays. In addition, a good vertex resolution and muon identification are important.

The LHCb vertex locator (VELO) provides a two–track vertex resolution of 110 μm in the z coordinate and a resolution of 40 μm on the track impact parameter. The LHCb trigger system has an efficiency of 80% for B meson decays containing muons [22]. The LHCb tracking system provides a reconstruction efficiency for tracks produced by muons from a B decay of 95%, with a 3% fraction of ghost[1]tracks and a momentum resolution of $dp/p \approx 0.4\%$ [23]. This yields an invariant mass resolution of 18 MeV/c^2 [21].

[1]Ghost tracks are wrongly reconstructed tracks that do not correspond to a particle.

Chapter 3

The LHCb Detector and Its Outer Tracker

3.1 LHCb

Due to the quantum mechanical nature of the interactions that are studied at particle accelerators and the very high energies involved, the timescales during which these interactions occur are very short. Most particles created in a proton-proton collision in the LHC do not live long enough to be measured directly, but decay. Their properties must be inferred from the properties of the secondary particles into which they decay. The lifetimes of the different types of particles vary over orders of magnitude; some decay before they can be observed and others can be observed directly. Many directly observable particles are unstable and will in turn decay; often inside the volume of the detector. The physics at LHCb is concerned with the reconstruction of consecutively decaying particles that have a B-meson as a primary particle.

Because of the light mass of B-mesons compared to the asymmetry in the energy of the proton constituents that interact, B-decays are heavily boosted. The particles from their decays predominantly leave the interaction region in the forward and backward directions, see figure 3.1.

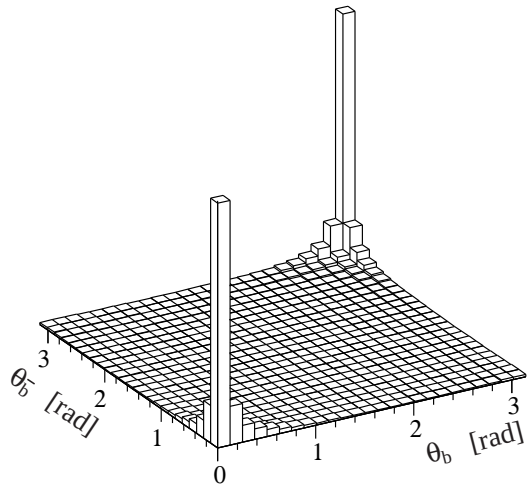

Figure 3.1: Polar angles of the b- and $\bar{b}$-hadrons calculated by the PYTHIA event generator.

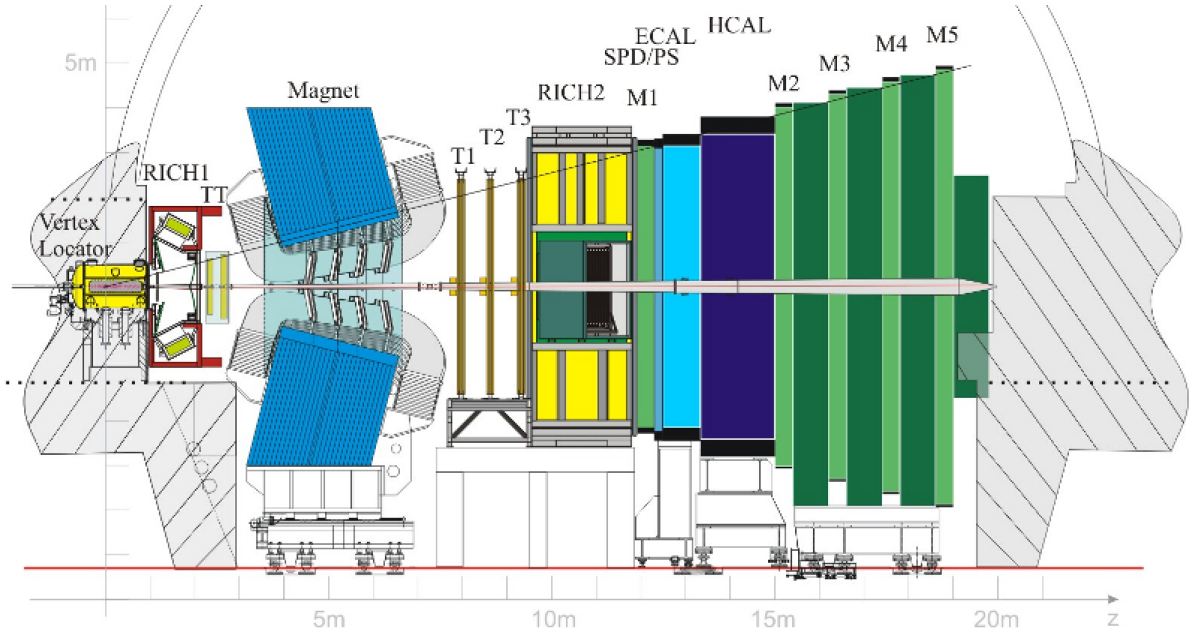

Figure 3.2: A schematic cross-section of the LHCb detector. The sub-detectors are shown, from left to right: Vertex Locator (VELO), Ring Imaging Cerenkov detector 1 (RICH1), Trigger Tracker (TT), Magnet, tracking stations T1-T3, Muon station 1 (M1), pre-shower calorimeters (PS and SPD), Electromagnetic Calorimeter (ECAL), Hadronic Calorimeter (HCAL) and Muon stations 2 through 5 (M2-M5).

As a result of this, LHCb is built as a single-arm spectrometer. The acceptance covers the angular range from 15 m rad up to 300 (250) m rad in the horizontal (vertical) plane. Figure 3.2 shows a schematic cross-section of the detector; the generally used coordinate system is also shown. It is a right-handed system with the origin at the interaction point. The z-axis is parallel to the beam and the positive or downstream direction is toward the muon system. The positive direction of the y-axis is the upwards.

A collision between two protons in which a B-meson is created results in approximately 30 primary charged particles in the LHCb acceptance. These particles will interact with detector material and create additional particles. On average, about 100 particles per event will traverse the detector. This high particle count, together with the high rate of collisions in the LHC, results in a very high flux of particles in the OT that needs to be handled.

For a complete reconstruction of the essential parts of an event that contains a B-meson, all relevant tracks must be reconstructed. The fraction of the detector channels that generates a signal in an event is called the detector occupancy.

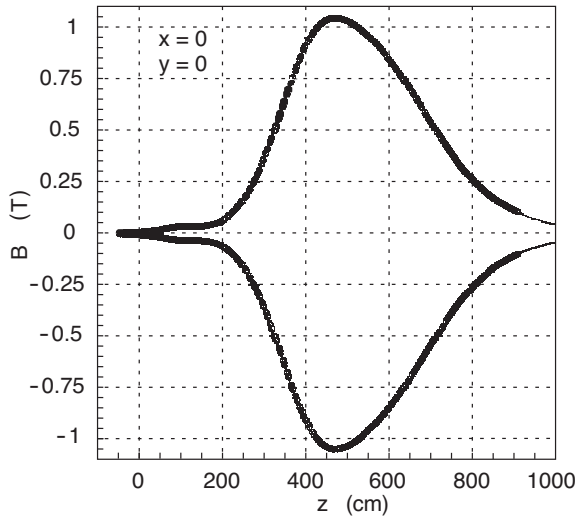

Figure 3.3: Magnetic field strength along the z-axis for the two different polarisations of the LHCb magnet.

3.2 Measurement of Particle Momenta in LHCb

To be able to correctly identify B-mesons and discriminate them from background, their invariant mass must be reconstructed with high precision. The main components in this reconstruction are the momenta of the particles into which the B-meson will ultimately decay. The LHCb tracking system is, therefore, designed for a high momentum resolution of typically $\delta p/p = 0.4\%$.

In order to determine the momentum of charged particles, they are deflected by a magnetic field. The bending power required for a momentum resolution of 0.4% for particles with momenta up to 150 GeV/c is about 4 T massuming a resolution of a few hundred μm for the tracking system. The magnetic field in LHCb is provided by a dipole magnet generating a field of about 0.5 T[24]. Figure 3.3 shows the magnetic field strength as seen by a test charge travelling along the z-axis.

The momentum of a particle is determined by the amount by which it is deflected by the magnetic field, which in turn is obtained by fitting a trajectory to the measurements made by the LHCb tracking detectors.

LHCb contains tracking detectors at four different areas along the path of a particle. The Vertex Locator (VELO) is the most sensitive tracking detector and is closest to the interaction point [25]. Its main purpose is a precise determination of the position of the decay vertex of the produced B-mesons, and of the impact parameter[1] of tracks from this vertex. It consists of twenty-one stations with two layers of silicon strip sensors each. The strips are arranged in concentric circles on one side and radially on the other. The width of the strips on the r–side increases with r. The single hit resolution of the VELO as measured in a beam test is shown in figure 3.4.

[1]The impact parameter is the shortest distance between a particle track and a point in space.

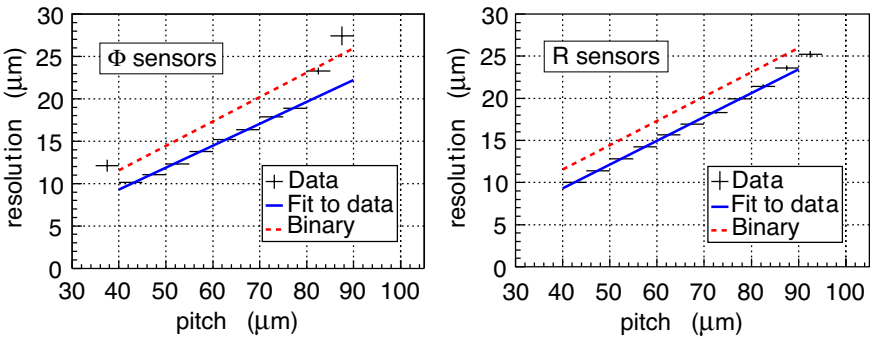

Figure 3.4: The single hit resolution of the LHCb Vertex Locator in the r and ϕ directions, as a function of the width of the silicon strips [3].

The next tracking detector is the Trigger Tracker (TT). As there is still an integrated magnetic field of 0.15 T mpresent between the VELO and TT detector; the deflection of particles in this field is used by the TT to provide the trigger with crude track momentum information with a resolution of $\delta p/p \approx 25\%$. The TT is also used in the reconstruction of particles decaying outside the VELO, and to measure trajectories of low-momentum tracks that are bent out of the detector acceptance.

Three tracking stations are installed behind the magnet. The particle density is highest in the inner region of these stations; to keep pattern recognition fast and reliable, a detector with a high granularity is required. The inner region is, therefore, covered by a silicon strip detector, the Inner Tracker (IT). The IT is surrounded by the Outer Tracker (OT), which is described in more detail below. The final element of the LHCb tracking system are five muon stations, whose main purpose is the identification and measurement of muons with high transverse momentum. Such muons are e.g. present in several CP-violating B-decays and play an important role in the search for physics beyond the standard model in rare decays of B-mesons.

3.3 Trigger System and Detector Readout

Under nominal LHC collision conditions, the minimal time between bunch crossings, and therefore collisions, is 25 ns. All readout electronics on the detector are built to collect signals inside time windows of this size. It is not possible to read out the detector this fast and store the data for all events. The majority of events also do not contain a B-meson pair and are, therefore, not of interest. A trigger system in three levels is installed to deal with these issues.

The first trigger system is the hardware or Level-0 (L0) trigger. It consists of very fast algorithms that are executed on dedicated hardware, which is built into the readout electronics. The L0 trigger is designed to reduce the event rate from 40 MHz to 1 MHz, at which rate the entire detector is read out. Data from all subdetectors is buffered in the readout electronics to allow for some delay in the L0 decision making process. Once an L0 trigger arrives for an event, data belonging to that event is collected and sent to the event filter farm on which the remaining and High Level Triggers (HLT1 and HLT2) are implemented.

The HLT1 software trigger is designed to confirm L0 decisions and reduce the event rate to $\approx$ 30 kHz. This rate is then further reduced to $\approx$ 2 kHz by HLT2. The events selected by HLT2 are stored on disk for further analysis.

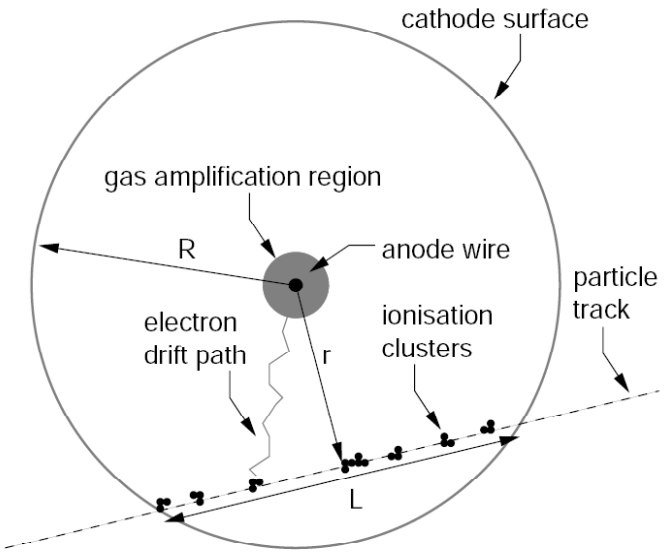

Figure 3.5: Schematic view of the detection principle of a straw tube. Electrons are liberated in small clusters along the track of an ionising particle and drift to the anode wire due to the presence of an electric field. Close to the wire, the field strength is sufficient to cause an avalanche. This avalanche is collected at the anode.

3.4 The Outer Tracker

For efficient track recognition, the occupancy must be as low as possible. Because of the high flux of particles, a low occupancy can only be obtained by building a detector with a high granularity. A gas-filled straw-tube detector was the natural choice to cover the large area of the OT, as it fullfills the needed compromises between granularity, resolution and financial restrictions.

The straws are arranged in layers and three stations contain each four layers, which are tilted with respect to the y-axis by angles of 0°, -5°, 5°and 0°, respectively. There are 48384 straws in the OT in total. The OT geometry is described in more detail in section 3.4.3.

3.4.1 Detection Principle

A charged particle moving through a gas transfers energy to the gas molecules by electromagnetic interactions ; if the energy transferred exceeds the ionisation potential of the gas molecule, a secondary electron may be liberated. If this electron has enough energy, it can in turn liberate additional electrons. Because this process takes place over a short range, a primary ionisation process will generally result in a cluster of electrons and ions.

In the presence of an electric field throughout the gas, free electrons and ions will not recombine, but drift in opposite directions along the field lines. Since electrons are much lighter than ions, their drift velocity is generally two orders of magnitude higher. If the electric field strength is high, electrons will be accelerated sufficiently to liberate additional electrons when they collide with molecules in the gas.

If the number of free electrons per collision exceeds unity, an avalanche of electrons will be created. This process is called gas amplification.

For straw tubes with an inner radius R, the electric field as a function of distance r to the anode wire of diameter r_a is given by:

$$E(r) = \frac{V}{r \ln \frac{R}{r_a}} \tag{3.1}$$

The field strength in such a field rises dramatically close to the anode wire, which causes gas amplification predominantly there. Any electrons entering this region will create an avalanche of secondary electrons, which are collected at the anode. Electronics can be used to detect the small current or the change in potential created in the wire.

Outside the amplification region, the presence of the field will cause electrons to drift toward the anode; most collisions with gas will cause the electron to be scattered elastically. The time it takes for an avalanche to be created in the amplification region is much shorter than the time it takes the electrons to drift to the anode. The time it takes the electrons to drift to the anode can therefore be used to determine the distance at which the primary particle passed the wire. A schematic overview of the detection principle of a straw tube is shown in figure 3.5

The OT is equipped with time to digital converters (TDC), which measure a time difference. The time at which the clock is started is set by the readout clock, and the clock is stopped once a signal is detected. There are several other contributions which influence the time difference, which is given by:

$$t_{tdc} = t_{TOF} + t_{drift} + t_{prop} + t_{el}. \tag{3.2}$$

Here, t_{TOF} is the time of flight of the particle, t_{drift} is the electron drift time, t_{prop} is the signal propagation time, and t_{el} is the electronic time offset. Once these contributions are known, equation 3.2 can be used to calculate the electron drift time, from which the drift distance, i.e. the distance between the particle track and the wire, can be obtained using the so-called $r(t)$–relation. This relation is discussed in section 3.4.7.

3.4.2 Outer Tracker Readout

The maximum drift time of electrons exceeds the 25 ns time interval between consecutive interactions. To be able to handle this effect, the Outer Tracker readout electronics is designed to store three 25 ns readout intervals per event for each trigger. This ensures that all drift times will be included in an event. This simultaneously leads to a higher occupancy due to the inclusion of hits belonging to earlier and later events, which causes a higher effective occupancy and thus complicates pattern recognition. It is unlikely that all hits that belong to a track have drift times large enough for all of of them to be included in an event to which they do not belong. Any hits that do get stored will also have their drift times reduced (or increased) by one or two times 25 ns. If such hits are assigned to a track by the pattern recognition, their contribution to the χ^2 of the track will be large. The track-fitting algorithms are designed to remove such hits, which further limits the problems due to spillover.

Another important feature of the entire LHCb readout system is the ability to store data of up to seven events before or after the events which caused the trigger. This allows for an easy time alignment of the readout system and was essential during the runs in which cosmic muons were recorded. This is discussed in more detail in chapter 4.

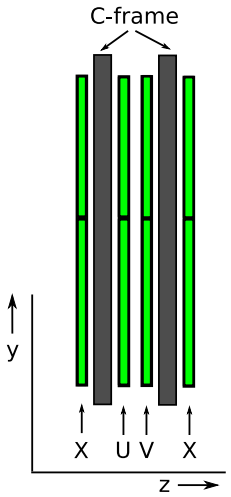

(a) Schematic side view of an Outer Tracker station.

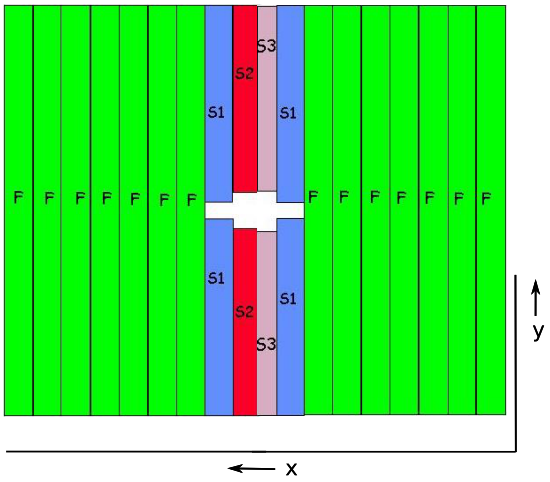

(b) Schematic front view of a vertical Outer Tracker layer.

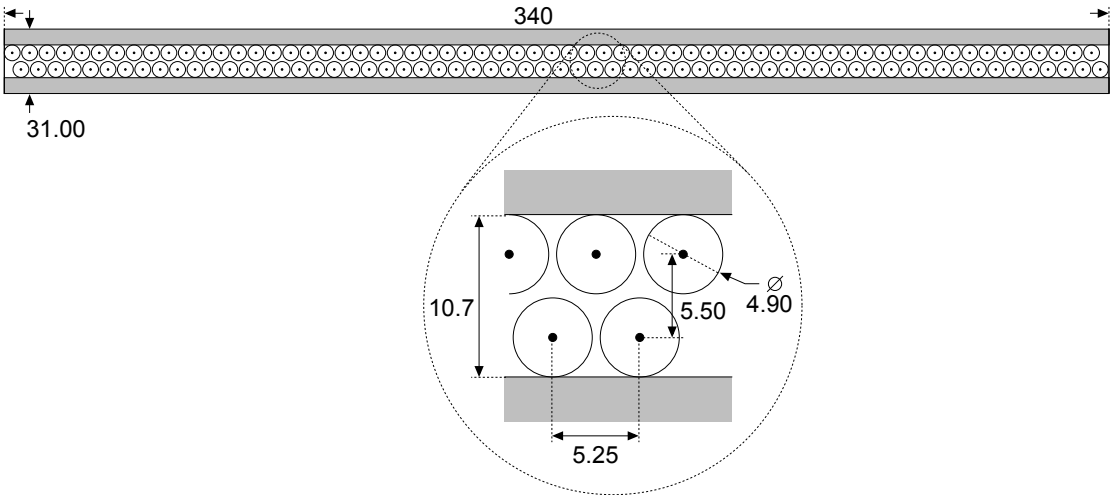

(c) Schematic cross section of an Outer Tracker module.

Figure 3.6: Schematic views of parts of the Outer Tracker.

3.4.3 Detector Geometry

A straw tube detector like the OT generally has a high resolution in directions perpendicular to the wire and low (or no) resolution along the wire. If the occupancy is high in in the direction along the wire, pattern recognition algorithms are more likely to wrongly assign hits to a track. To facilitate pattern recognition, half of the layers of straws is tilted five degrees with respect to the y-axis. This improves the resolution in this direction sufficiently to enable efficient pattern recognition without sacrificing too much resolution in the x direction.

The OT consists of three stations that are divided in four layers of 0°, -5°, +5°and 0°orientation[2]. The modules, which make up the layer, each contain two staggered layers of straws. This makes for a total of twenty four sensitive layers. The modules in all stations are attached to four steel C-shaped frames. Each frame holds half of the modules of one vertical and one stereo layer and

[2]The ±5° layers are called ”U” and ”V” layers, or ”stereolayers”; the 0° layers are called ”X” layers.

Module type	Number of Straws
F	128
S1 & S2	64
S3	32

Table 3.1: The number of straws that the various OT modules contain.

can be moved horizontally away from the beam pipe. This construction was chosen to be able to build the Outer Tracker independently of the Inner Tracker. The stations were assembled with the C-frames in an open position and are moved into their final position for operation; this construction facilitates maintenance. Every layer contains fourteen full-length (F-type) modules and eight short (S-type) modules. The S-type modules cover the area above and below the IT. Figure 3.6 shows a schematic view of several parts of the Outer Tracker.

The staggering of the two layers of straws in a module avoids insensitive areas in the acceptance. Even though the F-type modules cover the full height of the OT, the straws are split in the middle and both halves are read out at the outer edge of the module. This was done to halve the occupancy and to reduce signal propagation times. The amount of straws in a module layer for all types of modules is listed in table 3.1.

3.4.4 Time of Flight

After a collision, particles travel through the detector at speeds very close to the speed of light. It, therefore, takes them several nanoseconds to reach the Outer Tracker. This time of flight (TOF) contributes to the recorded time difference. The TOF depends on the length of the path of the particle, which most strongly depends on its angle with respect to the x and z-axes, and the layer under question.

3.4.5 Signal Propagation Time

The signal generated in the wire of a straw tube takes several nanoseconds to reach the electronics connected to the end of the wire. This propagation time depends on the vertical position, at which the particle hits a straw tube, and is included in the track-fitting algorithms. The signal propagation velocity has been measured to be 0.25 m/ns[26]. For a module length of 242.5 cm, this results in an average propagation time of 4.85 ns.

3.4.6 Electronic Time Offset

There are always differences in the lengths of cables connecting the read-out electronics to the data acquisition system. Since signals travel through cables at a velocity between 0.5 and 1 times the speed of light, differences in lengths larger than several centimetres contribute several nanoseconds to the time recorded. Small differences between individual read-out boards also cause time differences in the order of a few nanoseconds. The electronic time offsets are constants, they only change slightly once a different configuration of the electronics has been applied.

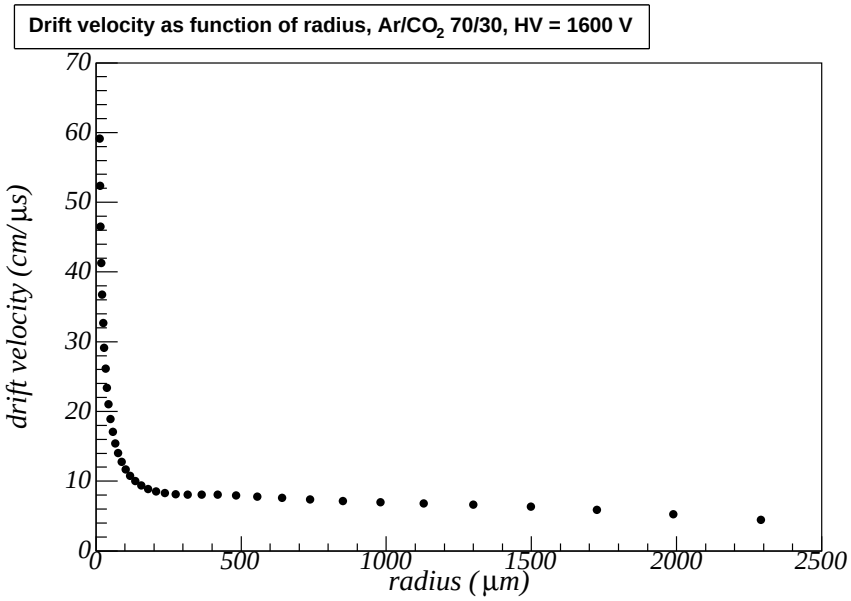

Figure 3.7: The drift velocity of electrons in Ar/CO_2 (70%/30%) as a function of the radius of an Outer Tracker straw tube and for a wire potential of 1600 V. This figure is courtesy of M. Blom [27].

3.4.7 $t(r)$–Relation

The time it takes electrons to drift to the anode strongly depends on their drift velocity in the gas of the detector. This velocity depends on the electric field strength; the relation is, however, non-linear due to the multitude of effects that contribute to the intensity and type of interactions between drifting electrons and gas molecules. These drift velocities are usually determined by numerical simulation. The drift velocity of electrons in the gas mixture used in the Outer Tracker, Ar/CO_2 (70%/30%), is shown in figure 3.7 as a funtion of the radius of an OT straw [27].

As can be seen from this figure, the drift velocity does not vary significantly for distances larges than 200 μm. The electric field strength as a function of distance to the anode is given by equation 3.1. Because the field only increases strongly very close to the anode wire, the drift velocity of electrons is near constant over most of the gas volume. This results in an almost linear $r(t)$–relation.

Instead of the $r(t)$–relation, its inverse is obtained from data. It is obtained from a comparison of the reconstructed distances between a track and its hits and the measured drift times for these hits. When the distance between a track and one of its hits is determined, the hit itself is not taken into acount. This procedure is discussed in more detail in section 5.8.

Any deviations from linearity in the $t(r)$–relation are modelled by adding higher orders terms to it. The $t(r)$-relation obtained from the measurements at the beam test of several OT modules in 2005 is shown in figure 3.8 [28].

As can be seen in figure 3.8, the $t(r)$-relation deviates most strongly from linearity at short drift times, which is expected since the electric field strength increases most in this region. It is described well by a polynome of second order:

$$t(r) = C_1 + C_2 |r| + C_3 r^2. \tag{3.3}$$

The coefficients of equation 3.3 obtained from the beam test data are -1.4, 8.2 and 2.4, respectively.

The constant component in the $r(t)$–relation, C_3, is fully correlated with the average electronic time offset for all modules. A natural choice for this component is zero, because it allows a straightforward interpretation of measured drift times.

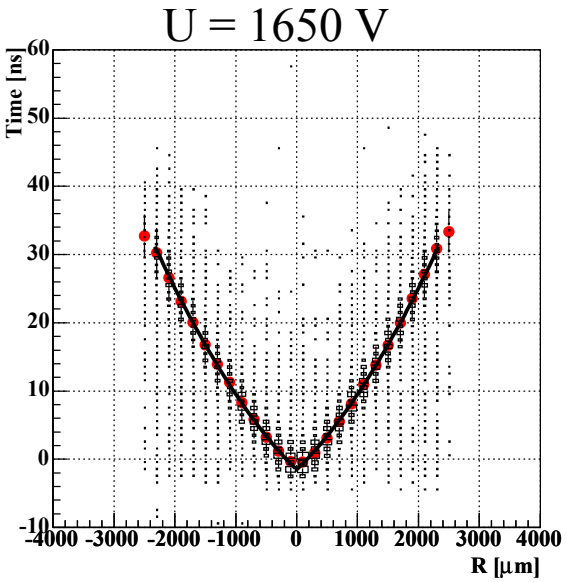

Figure 3.8: The $r(t)$-relation as it was obtained from the measurements in a beam of electrons at DESY in 2005 [28].

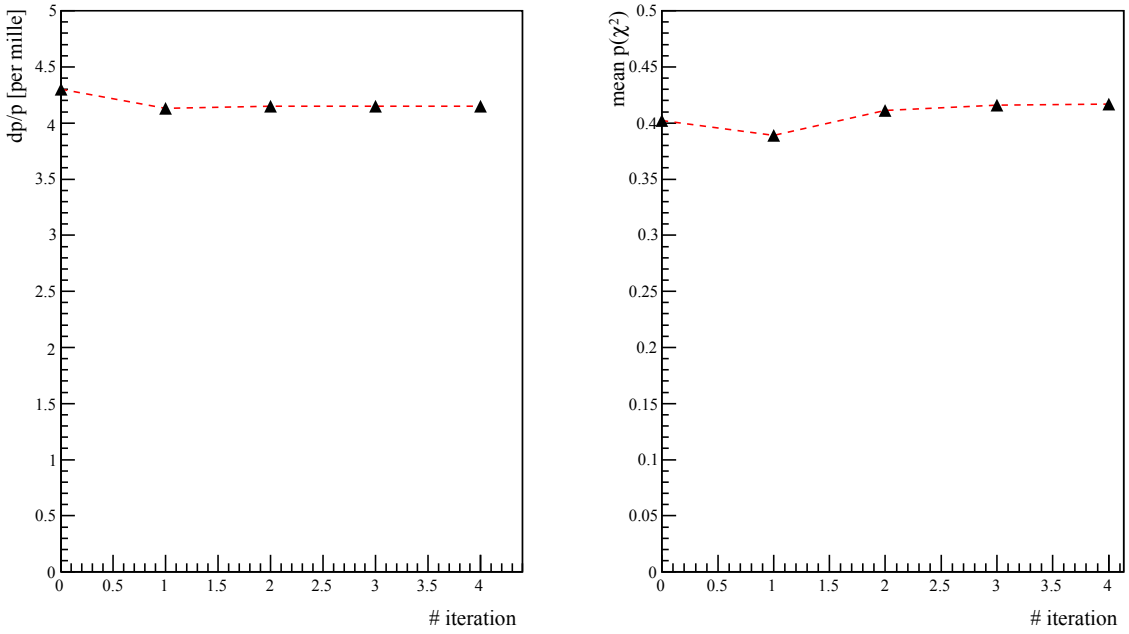

Figure 3.9: Momentum resolution (left) and mean $p(\chi^2)$ (right) as a function of the number of fit iterations [23].

3.4.8 Outer Tracker Requirements

The requirements for the LHCb Outer Tracker can be summed up as follows:

1. The resolution of the tracker should be sufficient to provide a momentum estimate with an accuracy of 0.4% for particle momenta from 2 GeV up to 100 GeV/c. A high momentum resolution reduces the error on the mass of reconstructed particles, which in turn facilitates the rejection of background events.

2. The channel occupancy must be sufficiently low; an occupancy lower than 10% results in a sufficiently efficient track reconstruction [29].

3. The performance of the tracker should not deteriorate over the foreseen lifetime of ten years.

In detailed studies of the reconstruction of tracks in LHCb [30, 31, 23], it has been shown that tracks can be reconstructed with the required accuracy; an OT resolution of 200 µm was assumed in these studies. The test of OT modules at DESY showed that this resolution can be obtained with a suitable setting of the high voltage [28].

The contribution of the resolution of the OT to the resolution of the entire LHCb tracking system is not easily modelled. Figure 3.9 shows the momentum resolution obtained after a number of iterations of the track fitting software. It is important to note that no drift time information is used in the first two iterations [32]. This implies that drift times need not be used to obtain the required momentum accuracy. The use of drift times and the consequent improvement of the OT resolution affects the efficiency of the pattern recognition, reduces the number of hits which are wrongly assigned to tracks and decreases the number of reconstructed tracks that do not correspond to a particle.

Chapter 4

Cosmic Muons in LHCb

Cosmic rays bombarding the earth's atmosphere cause extensive air showers [33]. Charged pions and kaons are created in copious amounts in these air showers and often decay to muons. Some of these muons will penetrate the rock above the LHCb experimental hall and traverse the detector; in the rest of this thesis, such muons are referred to as cosmic muons. As the LHCb-detector is a single arm spectrometer with a mostly horizontal acceptance, it is not well suited to measure tracks from cosmic muons, the majority of which has vertical trajectories.

There are several reasons why it is interesting to measure them anyway. Although simulations have provided valuable information on the performance of the LHCb subdetectors and the experiment as a whole, not all factors can be included in simulations. Some unforeseen factors may influence tracks from cosmic muons and studying this provides valuable information on the performance of subdetectors and reconstruction software. Cosmic muons are a perfect tool to study and commission a detector.

4.1 The Properties of Cosmic Muons Underground

The angular distribution of cosmic muons with energies around 3 GeV is proportional to $\cos^2\theta$, where θ is the zenith angle; it steepens for higher energies [15]. The LHCb detector is about 100 metres underground, and the 80 m of rock above it act as an absorber for cosmic muons. The pathlength through rock, L, that a cosmic muon encounters is approximately given by:

$$L \approx \frac{80}{\cos\theta}, \tag{4.1}$$

for $\theta < 70°$. The total energy loss as a function of the amount of matter traversed can be modelled by [34]:

$$-\frac{dE}{dX} = a + bE, \tag{4.2}$$

where a is the ionisation loss and b is the fractional energy loss due to radiative processes; both a and b vary slowly with energy. The quantity $\epsilon \equiv a/b$ (≈ 500 GeV in standard rock) defines a critical energy at which energy loss through ionisation equals that due to radiative processes.

If the energy dependence of a and b is neglected, equation 4.2 allows to work out the range R of muons by integration:

$$R = \int_E^0 \frac{\mathrm{d}E}{-\mathrm{d}E/\mathrm{d}x} = \frac{1}{b}\ln\left(1 + \frac{b}{a}E\right). \tag{4.3}$$

For not too large energies ($E < 100$ GeV) the ionisation energy loss dominates. In this case, $bE \ll a$ and therefore

$$R = \frac{E}{a}. \tag{4.4}$$

A muon of energy 100 GeV has a range of about 160 metre in rock.

If the energy spectrum of cosmic muons at sea level is known, equation 4.3 enables the calculation of the depth–intensity relation. The integral sea-level muon spectrum can be approximated by a power law

$$N\left(>E\right) \approx AE^{-\gamma} \tag{4.5}$$

and, using equation 4.3, the energy–range relation then becomes

$$N\left(>E,R\right) = A\left[\frac{a}{b}\left(e^{bR}-1\right)\right]^{-\gamma} \tag{4.6}$$

For high energies ($E_\mu > 1$ TeV, $bE \gg a$) the exponential dominates and one obtains

$$N\left(>E,R\right) = A\left(\frac{a}{b}\right)^{-\gamma} e^{\gamma bR} \tag{4.7}$$

This shows that for large depths, the number of muons decreases exponentially, which implies that the number of muons that traverse the earth and arrive from the bottom side of the detector is negligible.

4.2 Readout of Multiple Bunch Crossing Time Windows per Event

As described in section 3.3, the readout of the LHCb detector is divided in windows with a length of 25ns, which is also the smallest amount of time between two consecutive collisions of protons at the interaction point. If the trigger decides that an event is interesting, all data that is associated to that event is stored. Many factors, however, contribute to the time between the passing of a particle through a subdetector and the recording of the signal this causes.

The presence of such time delays requires a careful time alignment of subdetector components with respect to each other and the detector as a whole. To facilitate this, the LHCb electronics are capable of providing data for a number of time windows before and after a trigger has been given. This data is then stored as a part of the event for which a trigger occurred. This readout configuration can of course only be used if the rate of trigger signals is sufficiently low to ensure the availability of the additional readout bandwidth required.

When muons from cosmic rays are measured, timing effects play a larger role than they do under nominal operation conditions; the readout of multiple time windows is enabled by default in this case. Because the Outer Tracker measures a time difference it is affected strongly by any additional timing effects.

4.3 Event Time

Under nominal conditions, the start of a readout window in LHCb is provided by the central LHC clock, which is synchronised to the 25 ns interval between consecutive bunch crossings.

This clock is always available and is used to define the readout windows whenever data is collected, independant of the availability of collisions. The arrival time of cosmic muons with respect to this clock is random and is called the event time. Its distribution is expected to be flat between 0 and 25 nanoseconds and 0 otherwise.

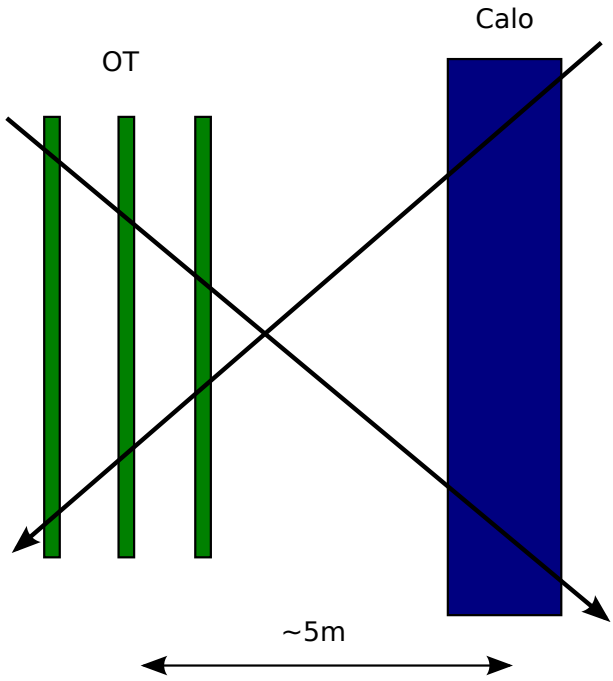

Figure 4.1: Schematic view of downstream and upstream tracks. Particles travelling downstream hit the Outer Tracker before they hit the Calorimeter, upstream particles hit the Calorimeter before the OT.

4.4 Time of Flight of Cosmic Muons

When operating under beam conditions, particles will travel through LHCb in the downstream direction. Cosmic muons, however, also traverse the detector in the upstream direction. Muons travelling in the downstream direction will hit the Outer Tracker before they hit the calorimeters, and vice versa for muons travelling upstream. The direction of a muon needs to be known to correctly determine its time of flight.

Since the rate of cosmic muons that traverse the LHCb-detector from bottom to top is negligible, cosmic muons are always assumed to enter the detector from above. This means that the angle between the the z–axis and the projection of a track on the y–z plane can be used to determine if the muon was travelling upstream or downstream. Figure 4.1 shows a schematic view of upstream and downstream tracks and the positions of the calorimeter and the OT.

Because the calorimeter is positioned several metres downstream of the OT, cosmic muons that hit both will always have a large zenith angle. Combined with the fact that muons always traverse the detector from top to bottom, this implies that muons travelling downstream will mostly hit the top of the OT, and muons traveling upstream will mostly hit the lower part. This is confirmed by figure 4.3b, which shows the distribution of y-coordinates for hits on upstream and downstream tracks.

Figure 4.3a shows the distribution of the angle of cosmic muons with respect to the z-axis and figure, which shows that there are roughly equal amounts of upstream and downstream tracks. This might imply that the larger amount of hits on track for upstream tracks is an effect of the reconstruction.

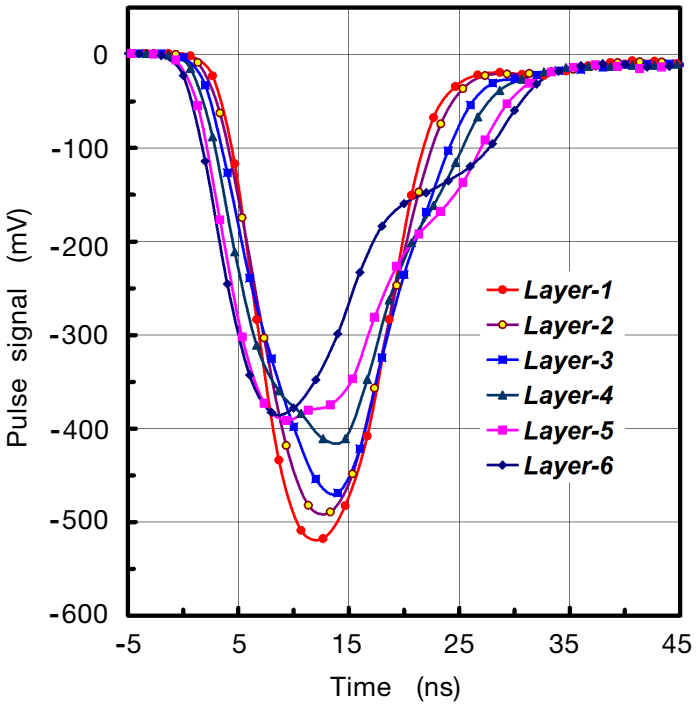

Figure 4.2: Signal shape of 30 GeV electrons in the calorimeter [3].

4.5 The Calorimeter as Trigger for Cosmic Muons

To obtain the highest possible rate of triggers for cosmic muons without requiring many changes to the Level-0 trigger configuration, the calorimeters were used as a trigger.

Since information of the calorimeters is used in the Level-0 trigger decisions under normal running conditions, an adjustment of thresholds was all that was needed to use the calorimeters as a trigger for cosmic muons. The thresholds were set up such that an energy deposit expected for a minimum ionising particle with an average energy of 50 GeV in the electromagnetic or hadronic calorimeters resulted in a trigger. This yielded a trigger rate of $\approx$ 10Hz, which is larger than the rate of useful events.

The shape of the calorimeter signal in time is very well known from simulations and tests with a particle beam [3]. Figure 4.2 shows the shape of the signal collected over time for 30 GeV electrons. Muons are minimum ionising particles and will, therefore, deposit far less energy in the calorimeters. The shape of the signal, however, is not expected to differ much from the one shown in figure 4.2.

The use of a threshold to distinguish cosmic muon events from noise has some side effects; if the signal of a cosmic muon in the calorimeter has a significant rise time before the threshold is reached, cosmic muons that arrive early or late in the readout window can cause a trigger for the previous or next bunch crossing. This causes the flat shape of the expected distribution of event times to be smeared with a resolution. The size of this effect depends on the height of the thresholds and the rise time of the spectrum, which in turn depends on the energy of each cosmic muon.

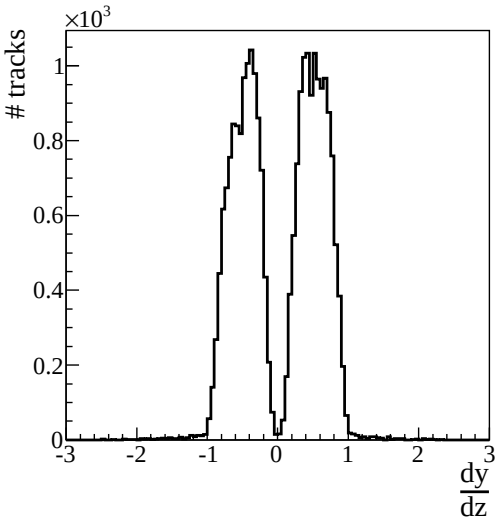

(a) Slope of tracks fitter without using drift times.

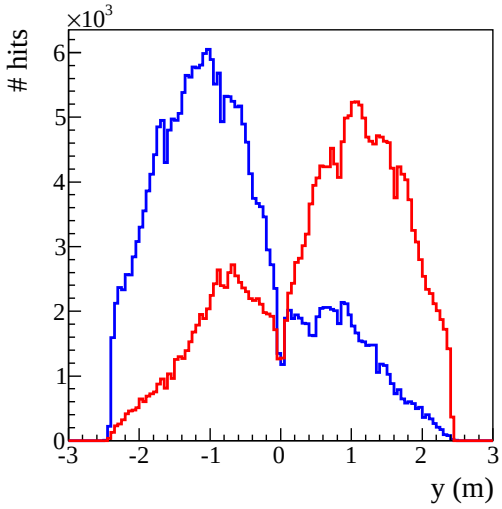

(b) y-Coordinate of hits on track for upstream tracks (blue) and downstream tracks (red).

4.6 Cosmic Muons in the Outer Tracker

When tracks of cosmic muons in the Outer Tracker are studied, equation 3.2 is no longer valid. The sign of the time of flight contribution is no longer always positive, and an extra contribution due the event time t_{ev} must be added. The tdc-time t_{tdc} for cosmic muons is given by:

$$t_{tdc} = t_{drift} + t_{prop} + t_{el} \pm t_{TOF} + t_{ev}. \tag{4.8}$$

If the event time contribution to equation 4.8 is not determined, an average contribution to all drift times of 12.5 ns with an error of $25/\sqrt{12}$ ns is expected. Taking an average drift velocity of 60μm/ns into account, this corresponds to an increase in position resolution of $\approx$ 430μm, which is much larger that the target resolution of $\approx$ 210μm.

Since none of the LHCb subdetectors is capable of measuring the arrival time of particles with respect to the readout clock directly, the event time must be determined separately. Several methods to obtain it are available and have been tried; they are discussed in their respective sections of chapter 5, and compared in section 5.6.

4.7 Multiple Scattering

Because the energy of cosmic muons in the Outer Tracker is approximately exponentially distributed, many will have low momenta. Particles with low momenta are more likely to undergo multiple scattering in the material of the OT. Because the momentum of cosmic muons cannot be measured in the OT alone, the amount of multiple scattering cannot be estimated.

Particles that undergo multiple scattering can not be reconstructed as well as particles that do not, since the assumption that their tracks are straight lines is no longer valid. Their χ^2 will thus be higher and the residuals of their hits larger. This generally causes tails in the distribution of the χ^2 per degree of freedom for all tracks and the distribution of residuals for hits on track. Only a cut on the χ^2 per degree of freedom can be used to limit the effect of multiple scattering on the residual distribution. In the following, a cut on the χ^2 per degree of freedom of 5 was used, unless stated otherwise.

Chapter 5

Calibration of the Outer Tracker

5.1 Calibration Procedure

The information most easily obtained from the cosmic data is how often all wires in the Outer Tracker have given a signal. Since the expected number of hits is very low, this gives an idea of the amount of noisy straws in the detector. This is discussed in section 5.2.

The simplest possible approach to fitting tracks uses only the position of the wires in the straws which were hit, ignoring any drift time information. Using this approach it is already possible to obtain information on the alignment of the OT. This is discussed in section 5.3.

Higher accuracy can be achieved by using drift times. This requires all terms of equation 4.8 to be known for each hit. The propagation time and the time of flight of a particle are known with sufficient accuracy once an initial fit of a track is made. The event time differs from event to event and must be obtained for each event. The different methods to obtain the event time that have been studied are described in section 5.5. The time offsets that are introduced by the electronics, t_{el}, are constant over the entire data set; their calibration is the subject of section 5.7.

The electronic time offsets, t_{el} are assumed to be constant over the data and once the event time is known for all events, any average deviation from the expected drift time value can be attributed to the electronic time offsets. Their determination is the subject of section 5.7.

Up to this point, the relation between the drift times of electrons and the distance they drifted was assumed to be linear. Following the argument of section 3.4.7 this assumption is valid up to first order. Once all contributions to equation 4.8 are known, the linearity of the $r(t)$-relation can be tested. This is discussed briefly in section 5.8.

5.2 Elimination of Noisy Straws

First, the amount of noise from Outer Tracker straws was studied. During a cosmic muon data run, about 10% of the events contain a cosmic muon which traverses the OT. A single track consists of 21 hits on average; see section 5.3.2 for a discussion of this number. This means that the average OT occupancy during a cosmic run is sufficiently low to accurately study its noise.

For each straw, the fraction of events in which it fired was recorded and is shown in figure 5.1. Five straws that fire in at most 15% of the events are not shown in the figure. As can be seen from this figure, the huge majority of the straws fires less than 0.05% of the events. This was

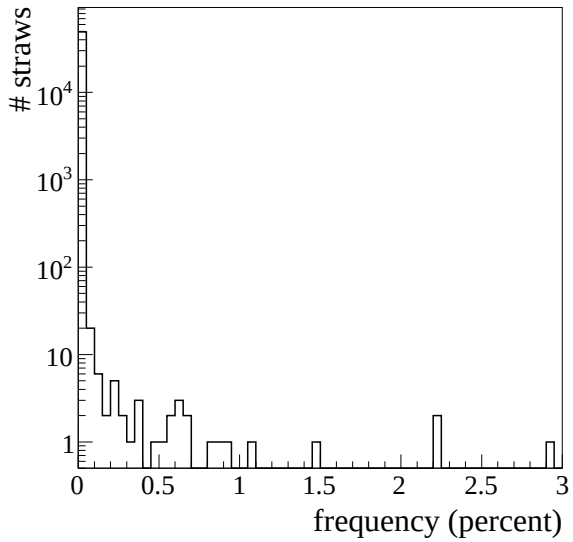

Figure 5.1: The frequency at which straws fired during a cosmic data taking run.

chosen as a limit above which a straw is said to be noisy. Under nominal conditions, noisy straws will be ignored by the pattern recognition and track fitting algorithms.

The OT is designed for nominal occupancy of the order of 10%, compared with which an additional occupancy of 0.05% due to noise is sufficiently low to not cause problems for the pattern recognition algorithms. Since 0.05% is an upper limit, the actual occupancy due to noise will be lower.

5.3 Track Fit without Drift Times

As a first step in analysing the tracks of cosmic muon in the Outer Tracker, only the position of wires was used to fit tracks. This simplifies the track fitting procedure and

5.3.1 Alignment Effects

To precisely reconstruct particle tracks, the position of all detector elements must be very accurately known. After the construction and the placement of a detector, surveys are conducted to determine the position of all subdetector elements. The accuracy of such surveys is, however, not sufficient to obtain the required accuracy on the position of the detector elements. After collisions have started, the detector will no longer be accessible and changes in its environment will cause slight deformations. It is therefore necessary to determine the relative position of all detector elements and the interaction point within it from collected data.

Tracks of particles that are known to be straight to a very good approximation can be used for relative alignment. If the position of a detector element is not as it is assumed to be, the reconstructed distance between a track and hits in that detector element will be biased. This biased will result in a higher than average contribution to the χ^2_{dof}[1] of the track. This in turn can be used to find the optimal value for any degrees of freedom in the position of detector elements.

[1] χ^2_{dof} is the χ^2 per degree of freedom

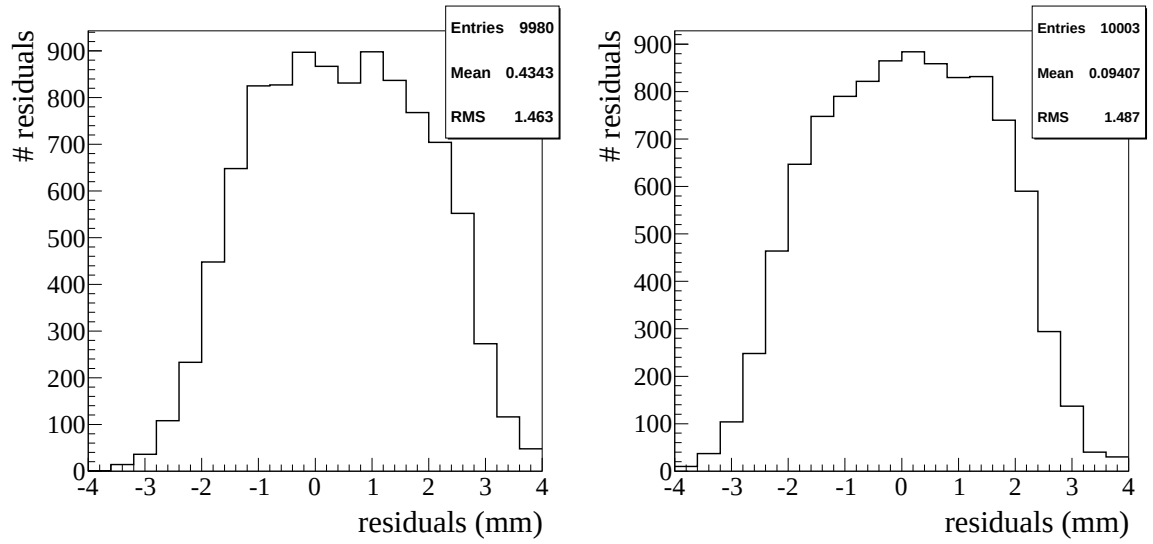

(a) Not aligned

(b) Aligned

Figure 5.2: Unbiased residuals for modules in quarter 0 of layer 0 in station 1.

Figure 5.2a shows the residuals of all hits in quarter 0 of layer 0 in station 1; a bias of 0.434 mm is clearly visible. The exact determination of the optimal values for all degrees of freedom in the positions of detector elements requires a complex alignment procedure, which is outside the scope of this thesis. In the remainder of the thesis, alignment data is used which was kindly provided by Jan Amoraal [35].

After including alignment information, figure 5.2b shows a residual of 0.09 mm for the same quarter as is shown in figure 5.2a.

5.3.2 Track Quality

Figure 3.6c shows a magnification of the cross section of an OT module. It can be seen that the insensitive areas between straws are 0.35 mm wide. To calculate the average number of hits expected in a module, a slice of a module between two adjacent wires in the same layer is considered. If only particles that traverse a module perpendicular to it's frontal surface are considered, the geometric probability that a particle traverses both straws is:$p_{dh} = 1-0.7/5.25 = 0.877$.

During the beam test of OT modules, the single hit efficiency, ϵ_{sh} was determined to be 0.98 [28]. The expected number of hits in a module is given by:

$$\langle n_{hits} \rangle = 2p_{dh}\epsilon_{sh}^2 + 2p_{dh}\epsilon_{sh}(1-\epsilon_{sh}) + \epsilon_{sh}(1-p_{dh}) \tag{5.1}$$

Since the Outer Tracker consists of 12 layers of modules, equation 5.1 yields an expected number of hits of 22.1. The configuration of the pattern recognition software is a large factor in the measured number of hits on track, so a deviation between the expected number of hits and the observed average number of hits, 20.8 from figure 5.3a, is to be expected.

The χ^2_{dof} of a fitted track is considered a good measure for the accuracy with which it was reconstructed. The average χ^2_{dof} gives an indication of how well errors are estimated: if errors are estimated correctly, it will be unity, if they are underestimated, it will be larger than unity

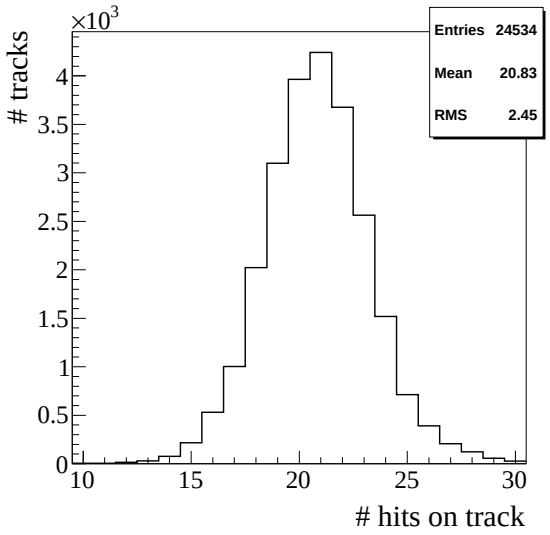

(a) The number of hits on track.

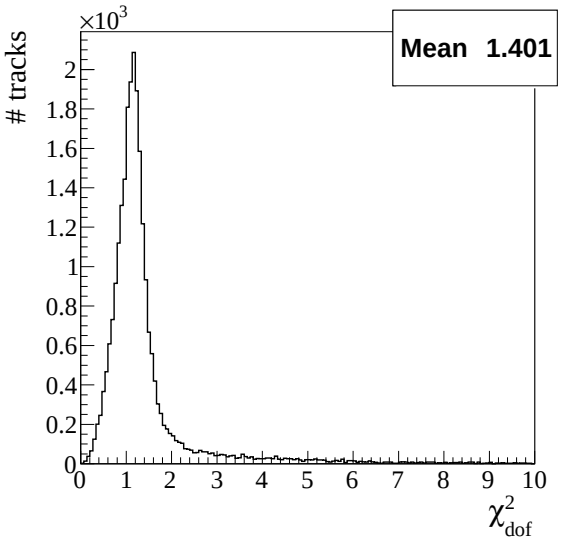

(b) Distribution of χ^2_{dof}.

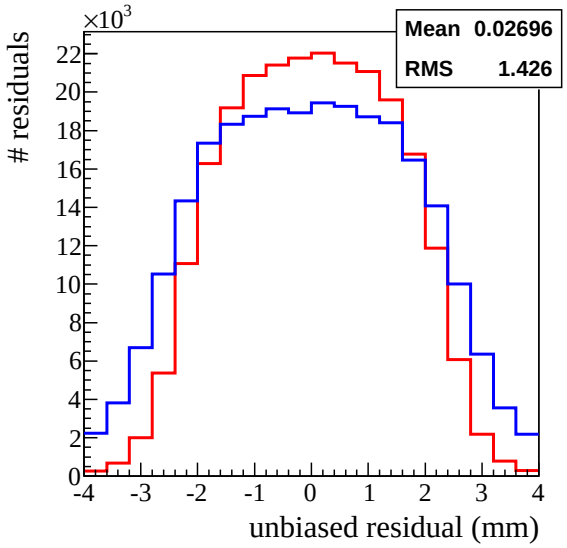

(c) Unbiased residuals for vertical layers (red) and horizontal layers (blue).

Figure 5.3: Results of fitting tracks without drift times.

and vice versa. Figure 5.3b shows the χ^2_{dof}–distribution for all analysed tracks. Its mean is 1.40, which indicates that errors are slightly underestimated (on average by 20%).

5.3.3 Track Resolution

Since particle tracks are expected to be distributed evenly over the width of a straw, the error on a measurement which only relies on the position of the wire is given by:

$$\sigma_{hit} = \frac{d}{\sqrt{12}}, \tag{5.2}$$

where d is the diameter of a straw. For the OT, d is 4.9 mm, which results in an expected error of $\sigma_{hit} = 1.41$mm.

To compare this prediction with data, the distance between points on a reconstructed track and the measured points can be used. A point considered must be excluded from the reconstruction to prevent unwanted biasing, in other words, unbiased residuals must be used. Figure 5.3c shows a histogram of the unbiased residuals for all hits on track. The distribution of residuals for vertical and stereo layers is shown. The RMS of the distribution for vertical layers agrees with the expected value of 1.41 mm.

5.4 Constant Contributions to the Drift Time

Several contributions to equation 4.8 contain a component which is constant for all events. Because no information is available which can be used to determine the origin of these components, only their sum is visible as a constant addition to all drift times. In the following paragraphs, the different sources of the constant components in equation 4.8 are described.

Time of Flight For nominal operating conditions, all particles originate from the interaction point inside the VELO; their time of flight is, therefore, always absolutely known. Since cosmic muons originate somewhere in the earth's atmosphere, their time of flight is unknown "a priori". To calculate the time of flight of a cosmic muon, a fixed plane of reference must be chosen, whose choice leads to a constant contribution to equation 4.8. In this thesis, a plain perpendicular to the z-axis, halfway between the electromagnetic and hadronic calorimeters has been used. Since the calorimeters provide the triggers for all events, this choice is expected to minimise this constant contribution and any possible side-effects it might have.

Electronic Time Offsets Electronic time offsets are caused by small differences in the read-out electronics. Since they are constant over a run, only their average value contributes to the constant component in equation 4.8.

$r(t)$-Relation The constant term in the $r(t)$-relation also contributes to the overall constant. Since a drift time of 0 ns naturally implies a drift distance of 0 mm, this term is expected to be absent. This is, however, not the case as will be shown in section 5.8. This term can be set to 0 by an appropriate choice of the other contributions. The severity of the side effects of this contribution depends on the method which is used to determine the event time.

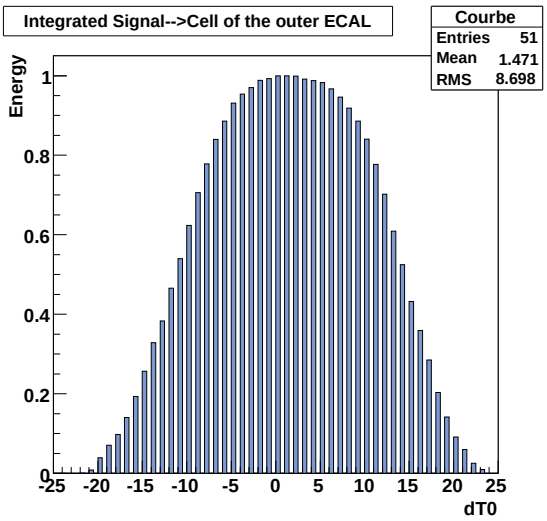

(a) The integrated signal in the calorimeter if a particle traversed the calorimeter at a time $dT0$ from the start of the readout window.

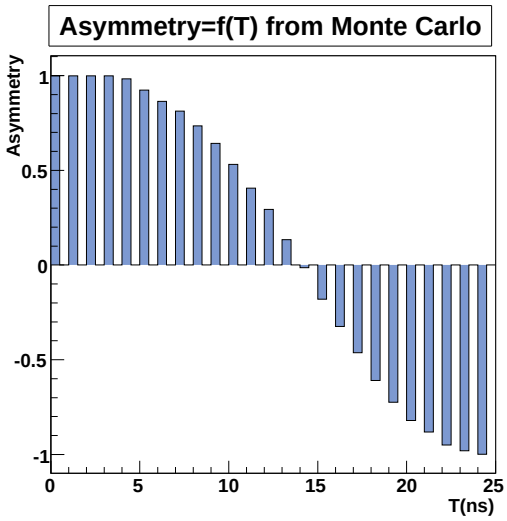

(b) The asymmetry between the integrated calorimeter signal contained in two consecutive readout windows.

Figure 5.4: Figures obtained from simulated data and kindly provided by Yasmine Amhis [36]

5.5 Determination of Event Time

Once alignment effects have been taken into account, the event time contribution to equation 4.8 is the largest source of errors on the determination of the electron drift times. Several methods of determining the event time have been suggested and are discussed in the following sections.

5.5.1 Event time from the Calorimeter

The shape of the signal produced by the photo-multiplier tubes (PMTs) of the LHCb calorimeters is shown in figure 4.2. The duration the signal is of the same order as the length of a data acquisition readout window. Figure 5.4a shows the integrated signal collected in a readout window if a particle traverses the calorimeter a time $dT0$ from the start of that readout window; it has been obtained from simulation [36]. $dT0$ is identical to the event time, t_{ev}.

The fraction of the signal that is not collected within a readout window, will be collected in the next readout window. This enables the construction of an asymmetry between the amount of signal collected in consecutive readout windows. This asymmetry is also a function of the time difference $dT0$ and is less sensitive to systematic effects. Figure 5.4b shows the shape of the asymmetry, obtained from simulation [36].

Data from consecutive readout windows is available for cosmic runs, and for each event the value of the asymmetry can be calculated. The shape of the asymmetry known from simulation is then used to determine the event time, t_{ev}. The calorimeter group provides software that implements this procedure. The event times obtained are shown in figure 5.5a. The χ^2_{dof}–distribution of the tracks which have an event time greater than 0 is shown if figure 5.5b. The distribution of unbiased residuals and their pull[2]distribution are shown in figures 5.5c and 5.5d respectively.

[2]The pull of a residual is the residual divided by its error.

5.5.2 Event Time from Average Drift Time

The event time changes all drift times by the same amount; thus, the average drift time can be used to obtain the event time. Since the average drift time depends on the sum of the constant contributions to equation 4.8, the event time obtained from it must be offset by the right amount. This correction is first set to the average drift time found when no event time correction is applied. This results in the event time distribution shown in figure 5.6a.

The average value of this distribution is shifted by about -15 nanoseconds from the average value of 12.5 nanoseconds expected for a distribution of event times as described in section 4.3. If 15 nanoseconds are subtracted from the offset, the mean χ^2_{dof} improves from 12.45 to 8.15; the improved distribution is shown in figure 5.6b. The distribution of unbiased residuals and their pull distribution are shown in figures 5.6c and 5.6d respectively.

5.5.3 Event time from Average Drift Time and Drift Time Residuals

The method of obtaining the event time from the average of the Outer Tracker drift times can be improved by also using information from the drift time residuals; residuals from only double hits, or all hits on the track can be used. Due to the staggering of the monolayers of straws in an OT module, double hits will have drift time residuals with opposite sign and are expected to provide a more precise correction.

The numbering of the straws in an OT module goes from 1 to 64 for one monolayer and from 65 to 128 for the other. To find a double hit in a module, the straw numbers of two straws in different monolayers can be used, if the difference between these numbers equals 64 or 65 straws, a double hit is found. Care needs to be taken to avoid double counting of double hits if a "triangle" of straws was hit. The results of using only double hits to correct the average event time are shown in figure 5.7.

Instead of using only drift time residuals of double hits to correct the event time, residuals of all hits can be used. Since not all hits in the OT are part of a double hit, this method will give more contributions to the drift time correction and is expected to give a more precise estimate of the correction. The results of using residuals of all hits on track to correct the average drift time are shown in figure 5.8

When all hits on track are used to correct the average drift time, the mean of the event time distribution obtained is closer to the expected value of 12.5 than if only double hits are used. The resolution and average χ^2_{dof} are, however, worse in this case, which shows that using only double hits to correct the average drift time gives better results.

5.5.4 Event Time from Track Fit

The track fitting software can also be used to fit the event time. Since this method uses information from all hits on a track and automatically takes errors on the measurements into account, it is expected to perform best. Figure 5.9 shows the results of using this method to obtain the event time.

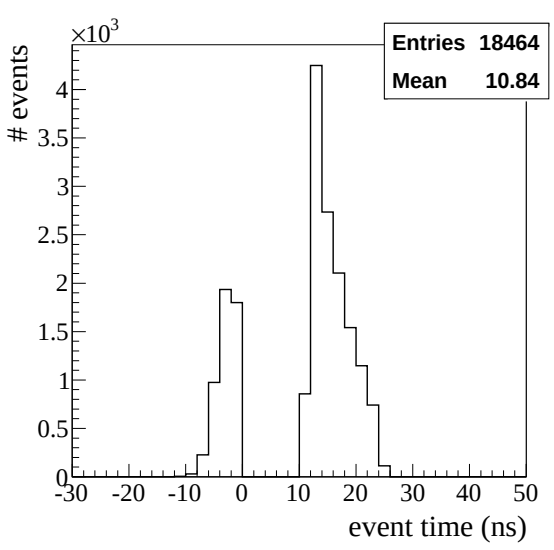

(a) Distribution of event times.

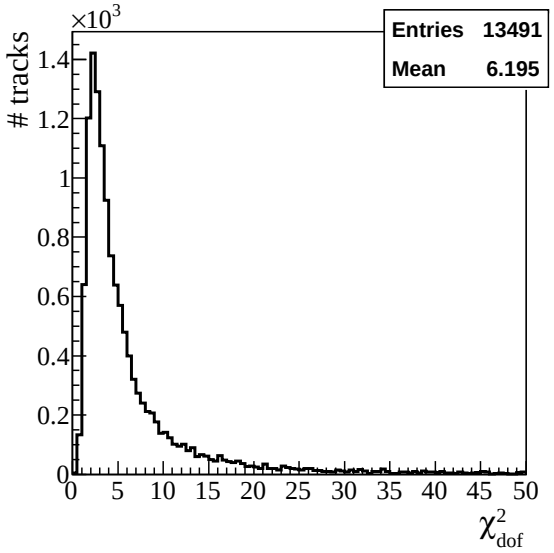

(b) χ^2_{dof}–distribution of tracks.

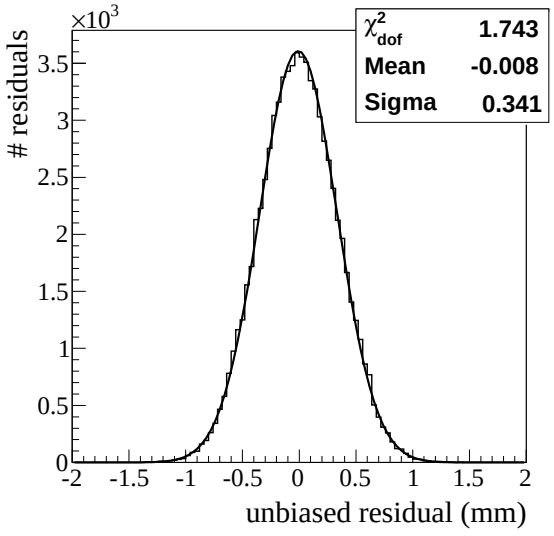

(c) Distribution of residuals for hits on track. The distribution has been fitted with a Gaussian.

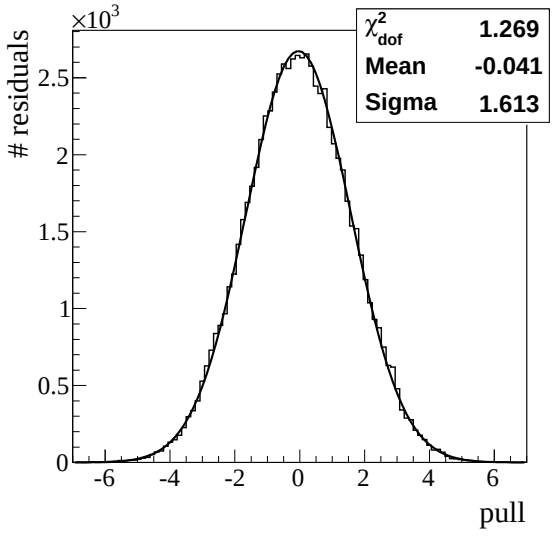

(d) Residuals pull distribution for hits on track.The distribution has been fitted with a Gaussian.

Figure 5.5: Results of using drift time information in the track fit; the calorimeter software has been used to obtain the event time.

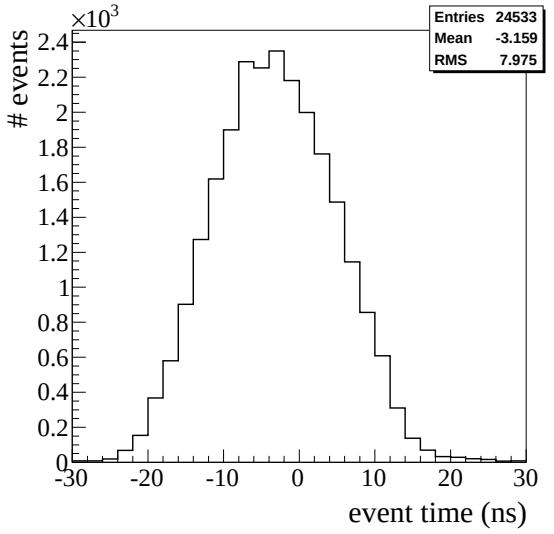

(a) Event times obtained from the average drift time.

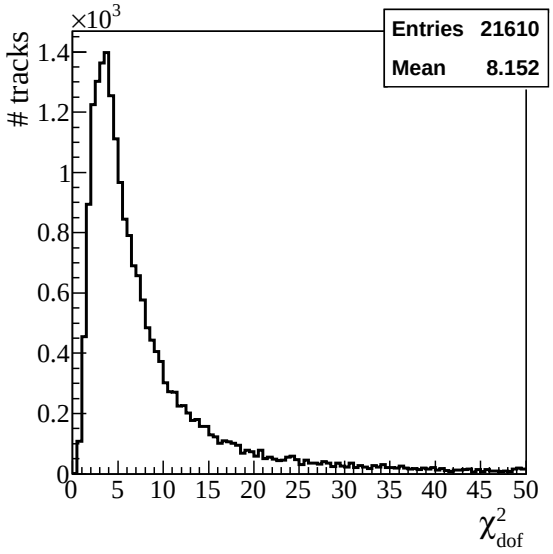

(b) χ^2_{dof}–distribution of tracks. Drift time information was used in the track fit and the event time was obtained from the average drift time.

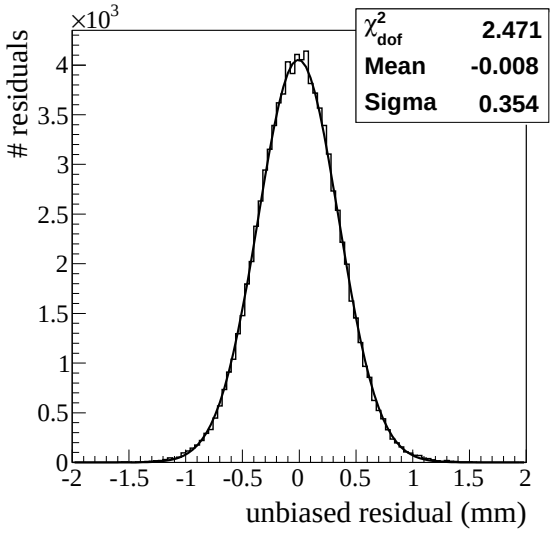

(c) Distribution of residuals for hits on track in vertical layers of the Outer Tracker. Drift time information was used in the track fit and the event time was obtained from the average drift time. The distribution was fitted with a Gaussian.

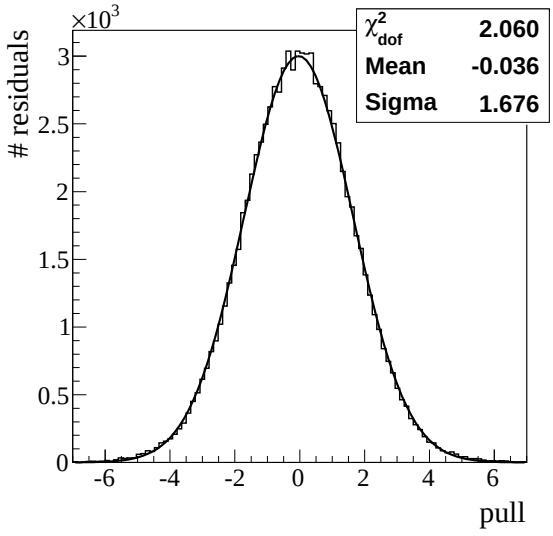

(d) Pull distribution of residuals for hits on track in vertical layers of the Outer Tracker. Drift time information was used in the track fit and the event time was obtained from the average drift time. The distribution was fitted with a Gaussian.

Figure 5.6: Results of using drift time information in the track fit; the event time has been obtained from the average drift time.

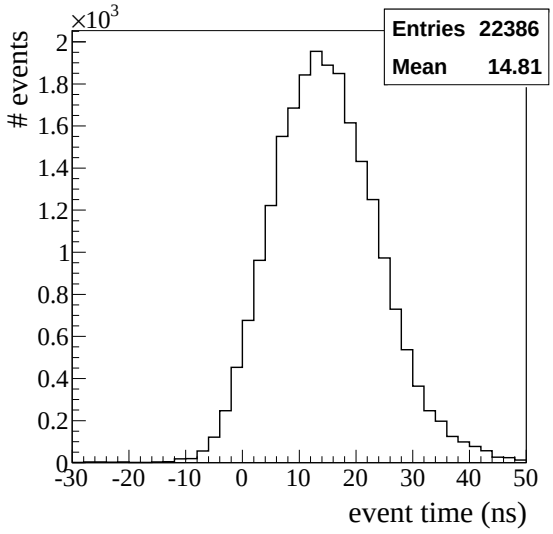

(a) Distribution of event times obtained from the average drift time, corrected using drift time residuals from double hits.

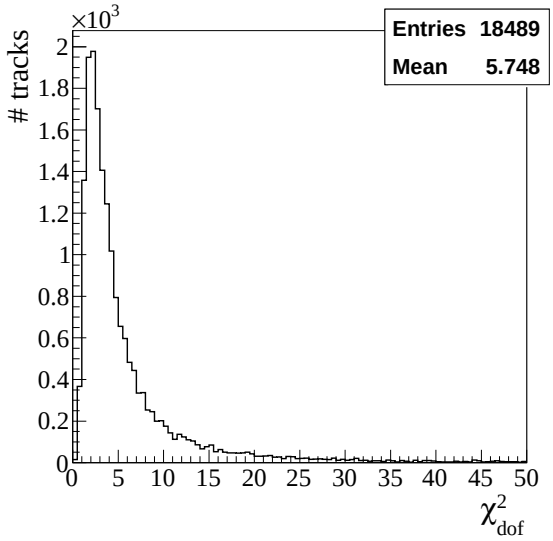

(b) χ^2_{dof}–distribution of tracks.

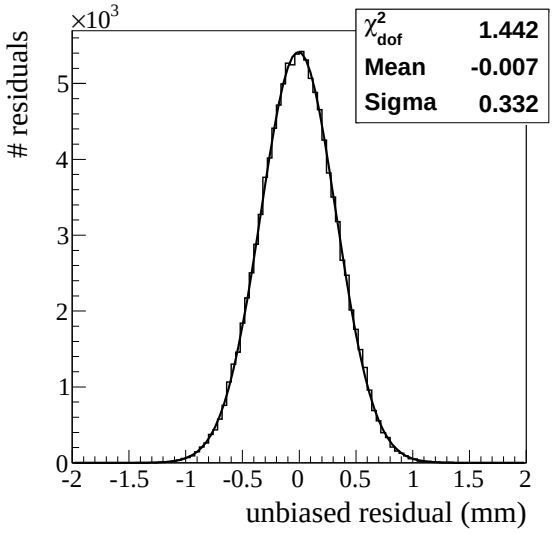

(c) Distribution of residuals for hits on track in vertical layers of the Outer Tracker. The distribution was fitted with a Gaussian.

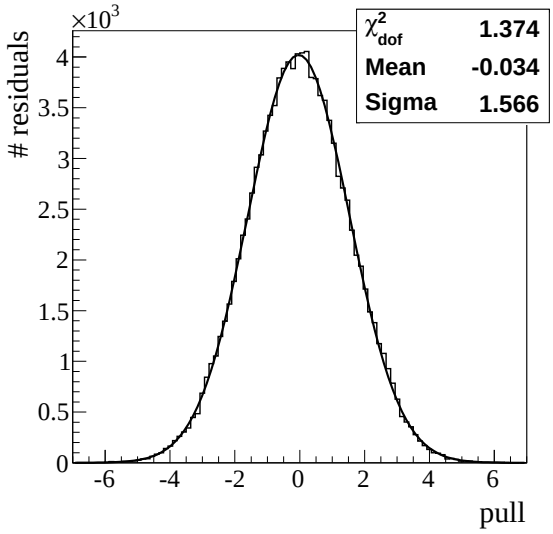

(d) Pull distribution of residuals for hits on track in vertical layers of the Outer Tracker. The distribution was fitted with a Gaussian.

Figure 5.7: Results of using drift time information in the track fit; the event time has been obtained from the average drift time, corrected using drift time residuals from double hits.

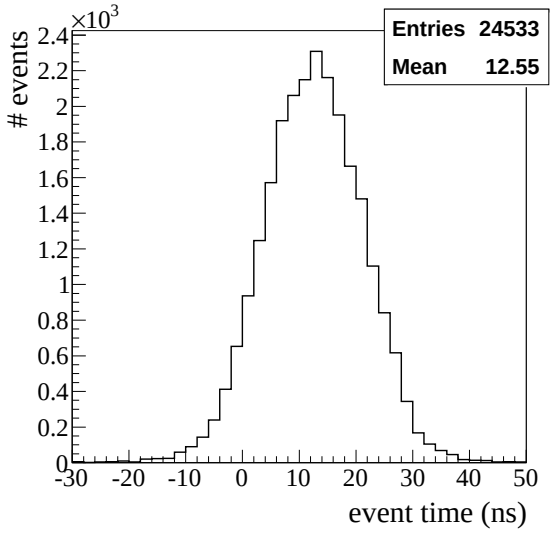

(a) Event times obtained from the average drift time, corrected using drift time residuals from all hits.

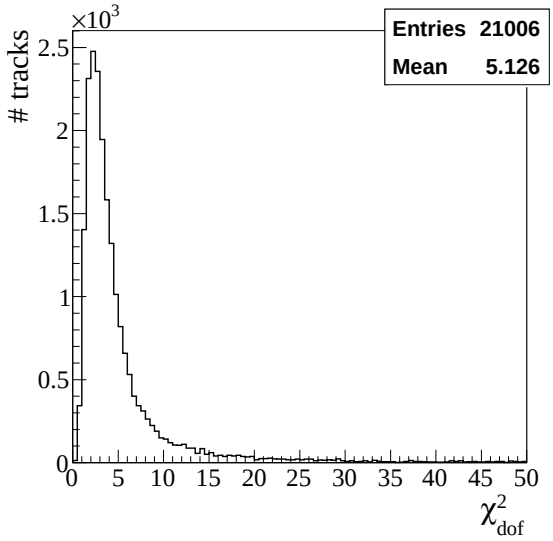

(b) χ^2_{dof}–distribution of tracks.

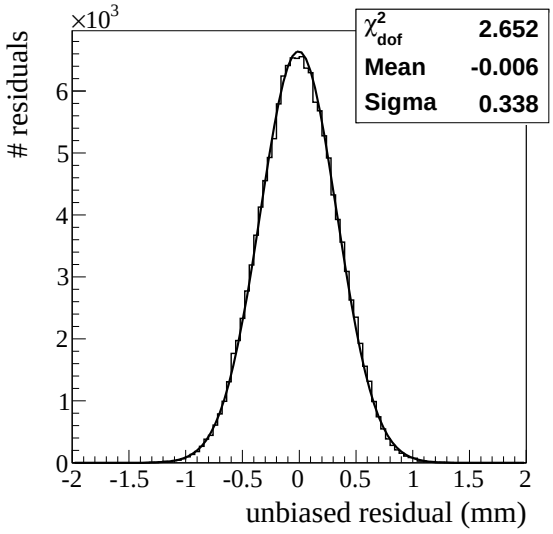

(c) Distribution of residuals for hits on track in vertical layers of the Outer Tracker. The distribution was fitted with a Gaussian.

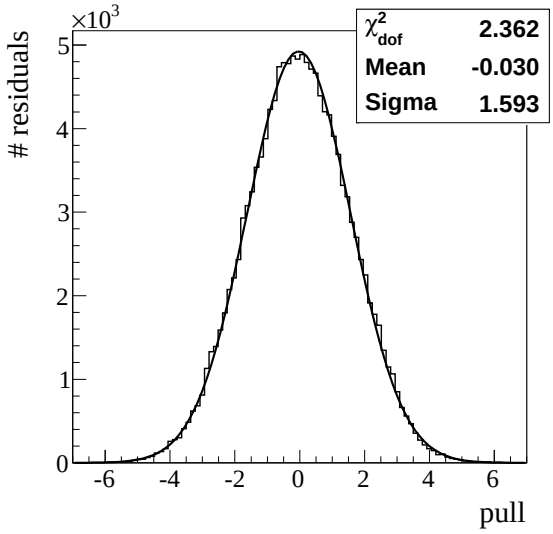

(d) Pull distribution of residuals for hits on track in vertical layers of the Outer Tracker. The distribution was fitted with a Gaussian.

Figure 5.8: Results of using drift time information in the track fit; the event time has been obtained from the average drift time, corrected using drift time residuals from all hits.

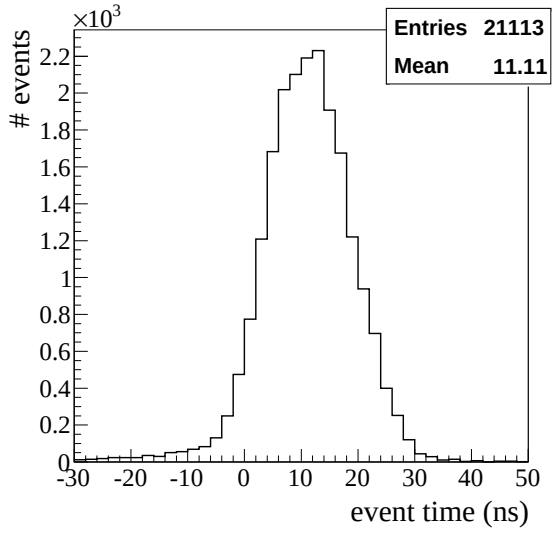

(a) Event times obtained from the track fit.

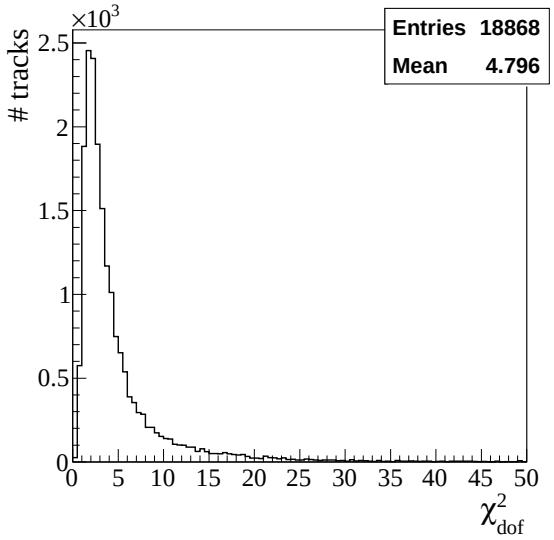

(b) χ^2_{dof}–distribution of tracks.

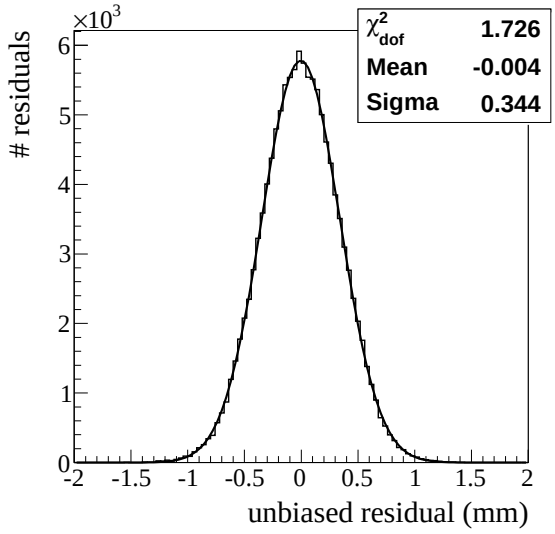

(c) Distribution of residuals for hits on track in vertical layers of the Outer Tracker. The distribution was fitted with a Gaussian.

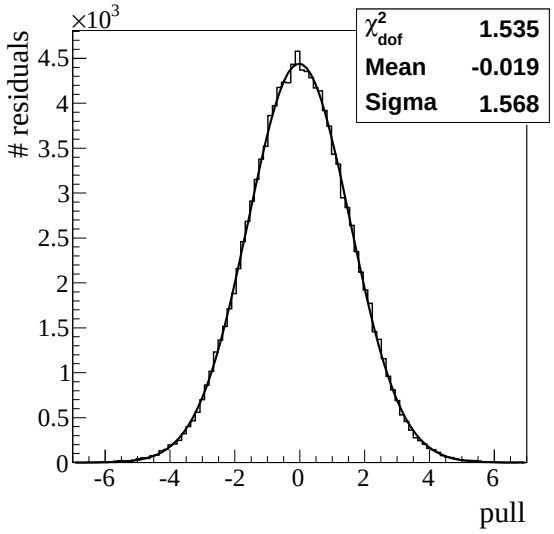

(d) Pull distribution of residuals for hits on track in vertical layers of the Outer Tracker. The distribution was fitted with a Gaussian.

Figure 5.9: Results of using drift time information in the track fit; the event time was obtained directly from the track fit.

5.6 Comparison of Methods to Obtain Event Time

Two different types of comparisons are described in this section: comparison of the quality of the tracks yielded by using the different methods, and consistency checks. The consistency checks also give an indication of the resolution of the different methods.

5.6.1 Comparison of Track Quality

When comparing the quality of tracks obtained using the different methods the mean χ^2_{dof} of all tracks and the resolution obtained with the different methods are considered. To a lesser extent, the width of the unbiased residual pull distribution and the amount of tracks are also taken into account. Table 5.1 summarises these values.

5.6.2 Comparison of Event Time from Calorimeter and Track Fit

Figure 5.10a shows a two dimensional histogram of event times obtained from the calorimeter software plotted versus event times obtained from the track fit. A Gaussian is fitted against the projection of each bin on the horizontal axis on the entire vertical axis, the mean and sigma of this Gaussian are shown if figure 5.10b. This graph was fitted with a first order polynomial.

If both methods give the same result, the constant term of this polynomial should be 0 and its linear term 1. This is not observed, which indicates that the calibration of the shape of the asymmetry, which was obtained from simulation, is not entirely accurate.

5.6.3 Comparison of Event Time From Average Drift Time and Track Fit

To further test the consistency of the different methods, the method that uses the average drift time and corrects it using drift time residuals of all hits on track is compared to the track fit method. The expected range of event times for both methods lies between 0 and 25; these limits result in more noise of higher values for small event times and vice versa for large event times.

To determine the shape of the distribution, event times are once again projected on the vertical axis for each bin on the horizontal axis. Asymmetric noise would bias the subsequent fit with a Gaussian of these projections to higher mean values for low event times and vice versa. To alleviate this problem, the entire distribution is first rotated around the origin over an angle of 45 degrees; the resulting 2 dimensional histogram is shown in figure 5.11a.

The same procedure as described in section 5.6.2 was followed to produce figure 5.11b. The results of the fit with a first order polynomial of this graph agrees well with a good consistency of the two methods, and a change of approximately 1 nanosecond of the range of 25 nanoseconds is acceptable.

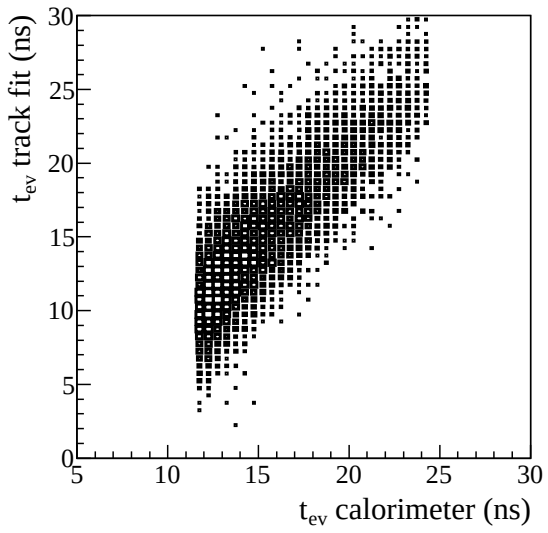

(a) Event times obtained from the calorimeter versus event times obtained from the track fit.

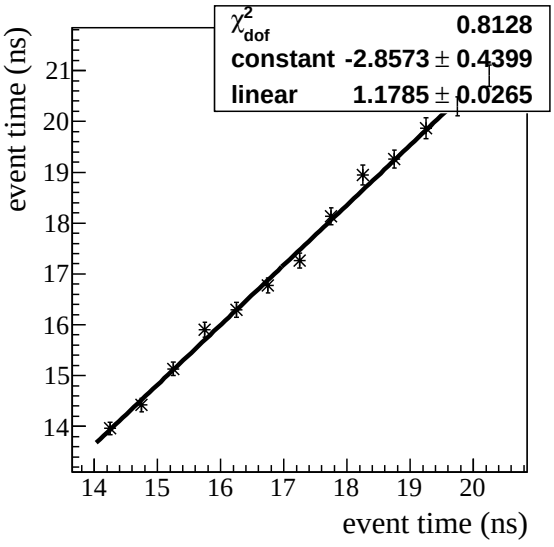

(b) Mean value of a Gaussian fitted to the projection of each bin on the horizontal axis on the entire vertical axis of figure 5.10a. A first order polynomial was fitted to the data points.

Figure 5.10: Comparison of methods to obtain the event time: calorimeter versus average drift time.

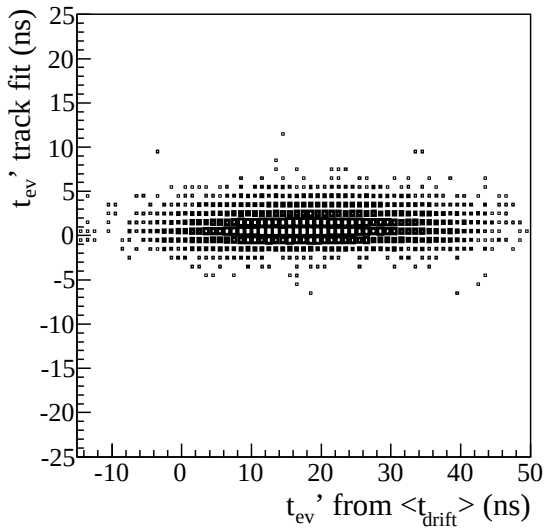

(a) Event times obtained from the average drift time, corrected using all hits versus event times obtained from the track fit, the entire plot was rotated clockwise over an angle of 45 degrees.

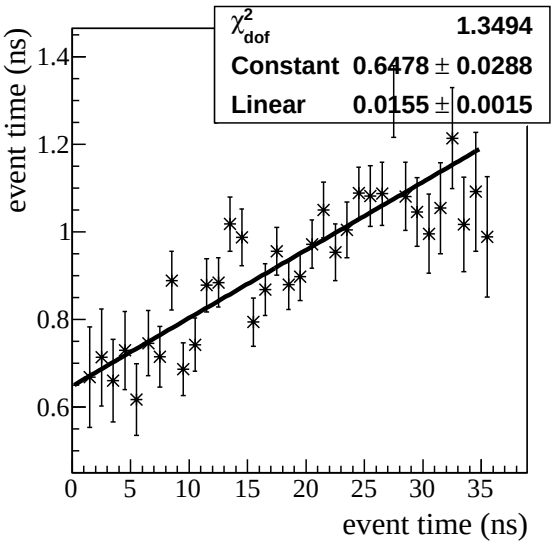

(b) Mean value of a Gaussian fitted to the projection of each bin on the horizontal axis on the entire vertical axis of figure 5.11a. A first order polynomial is fitted to the data points.

Figure 5.11: Comparison of methods to obtain event time: average drift time corrected using drift time residuals of all hits versus track fit.

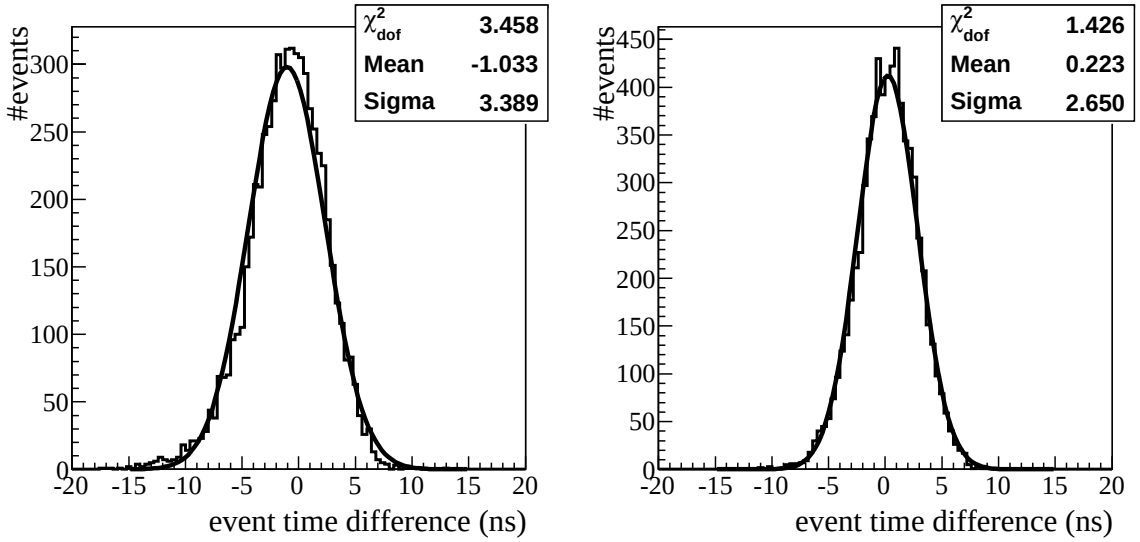

(a) Distribution of differences of event time obtained from the calorimeter and from the average drift time; the average drift time has been corrected using time residuals of double hits.

(b) Distribution of differences of event time from the calorimeter and event time the from track.

Figure 5.12: Distributions of diffences in event time obtained with the calorimeter and using drift times. The distributions have been fitted with a Gaussian.

5.6.4 Discussion and Choice of Method

If two methods to obtain the event time are independent, the differences between the derived event times are of purely statistical origin and should follow a Gaussian distributed around 0. The width of this distribution is the quadratic sum of the resolution of both methods. The Gaussian fit to the distribution shown in figure 5.12a has a χ^2_{dof} of approximately 3, indicating that the origin of the differences is not purely statistical. The Gaussian fit to the distribution shown in figure 5.12b is more consistent with a statistical origin of differences.

The width of the distribution of differences between the methods using the track fit and the calorimeter (figure 5.12b) is narrower than the distribution shown in figure 5.12a. This implies that the track fit method has a better resolution than the method that uses the average drift time, corrected using drift time residuals from double hits. The distribution shown if figure

method	mean χ^2_{dof}	resolution µm	pull width	#tracks ($\times 10^3$)
calorimeter	6.20	341	1.61	13.5
$\langle t_{drift} \rangle$	8.15	354	1.68	21.6
$\langle t_{drift} \rangle$ double hits	5.75	332	1.57	18.5
$\langle t_{drift} \rangle$ all hits	5.13	338	1.59	21.0
track fit	4.80	344	1.57	19.0

Table 5.1: Values used to compare different methods of obtaining event times.

5.12b also has a shape that is better described by a Gaussian, which implies that the track fit method is less likely to suffer from systematic effects.

The fact that the mean χ^2_{dof} for the calorimeter method is higher than it is for the other methods, discards it as the method of choice. Out of the other methods, the track fit method intrinsically treats the errors on drift times correctly, has the best mean χ^2_{dof} and has the best event time resolution between the differenct methods that use drift times. This leads to the choice to use the track fit method for the work described in remainder of this thesis. To ensure that any hidden effects are not overlooked, cross checks are always made using the other methods.

If the event time is not determined, an addtional error on the drift times of $25/\sqrt{12} = 7.2$ ns is incurred. The fact that the combined resolution of the calorimeter and track fit methods is approximately 2.6 ns indicates that using the event time will considerably improve the quality of tracks fitted using drift times.

5.7 Calibration of Electronic Time Offsets

The readout electronics for all modules are slightly different and might have slightly different optimal settings. These differences cause differences in the time it takes the electronics to process a hit in a wire. These differences are called t_{el} or t_0 and are assumed to be constant as long as the electronics are not reconfigured.

5.7.1 Method

To obtain the t_0 of a straw, its average drift time residual can be used. The electronics are such that a group of 32 wires is connected to the same set of electronics - an OTIS - of which there are four per module. Since there were not enough hits in the data to calibrate a separate t_0 per straw, they were calibrated per OTIS by taking the average drift time residual for all straws that belong to a certain OTIS.

Once the average drift time residual, r_{av}, for an OTIS is known, the t_0 is given by: $t_0 = -r_{av}$. The process of determining the average drift time residual and setting its corresponding t_0 value for all boards was repeated several times. After each iteration, the difference of each t_0 compared to its previous value was recorded. The width of the distribution of these differences for subsequent iterations is a measure for the convergence of the procedure. It is expected to become smaller until a constant value is reached, which gives the error on the t_o's.

5.7.2 Results

The evolution of the width mentioned in the previous paragraph is shown in figure 5.13a by plotting the RMS of the distribution of differences versus the number of the iteration. The distribution of differences after six iterations is shown in figure 5.13b. After the seventh iteration, no difference between subsequent values of a t_0 can be observed for most OTISs. Figures 5.13c and 5.13d show the values of the $t_0 s$ and their distribution after six iterations.

The effect of the calibration of t_0s per OTIS on the quality of the track fit is shown in figures 5.14a, 5.14b and 5.14c.They show the χ^2_{dof} distribution for all tracks, unbiased residual distribution for hits on track and the pull distribution for these residuals, respectively.

By comparing these to figures 5.9b, 5.9c and 5.9d, it can be seen that the average χ^2_{dof} has improved and the width of the residuals distribution has decreased, which shows the positive effect of the calibration.

5.7.3 Discussion

Using the obtained time offsets, the resolution improves becomes and average 341 μm. The quality of the fit of a Gaussian to the pull distribution has decreased, as can be seen from the behaviour of the χ^2_{dof} of the fit, which increases from 1.5 to 2.2. This may indicate that some "noise" which was previously present and caused a better agreement with a Gaussian distribution is now removed, and (or) that there is still a systematic effect that distorts the shape of the pull distribution. One candidate for this effect is the fact that until now, a linear $r(t)$-relation is used, while it is known from the results of the beam test to be non-linear [28]. This is discussed in the next section.

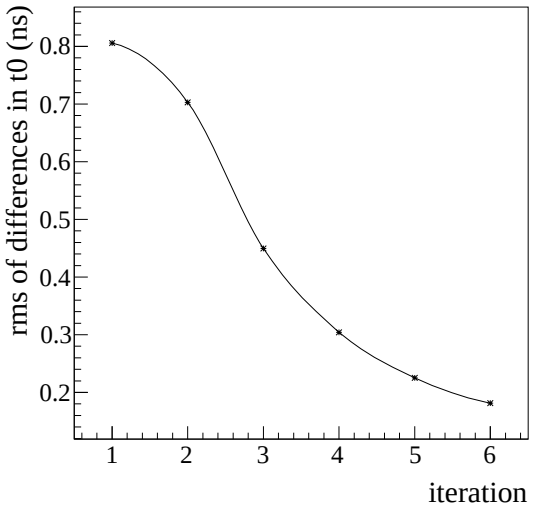

(a) RMS of the distributions of differences between T0s from each iteration to the next.

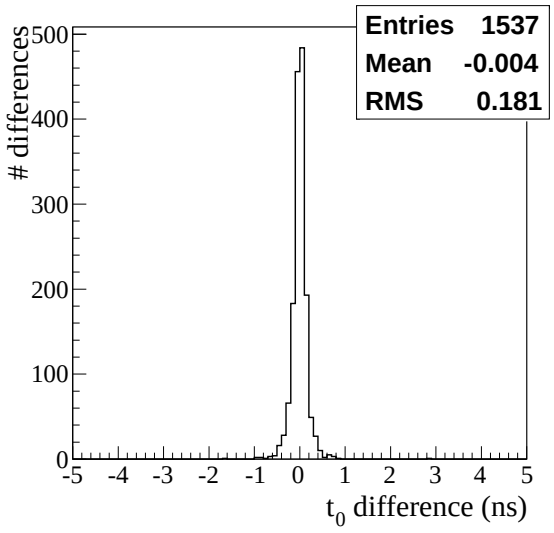

(b) Distribution of differences between the 5th and 6th iterations.

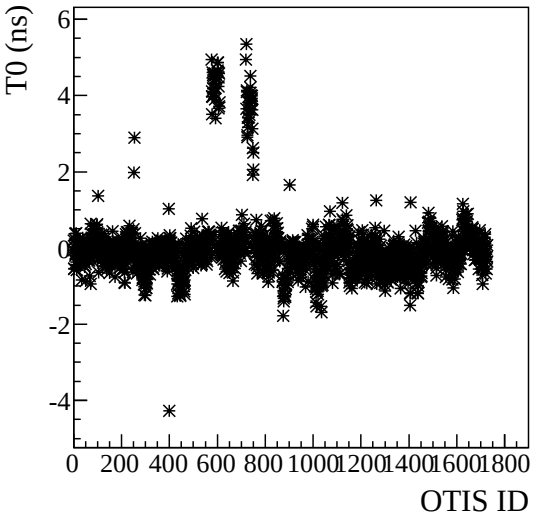

(c) Value of t0 per OTIS. The horizontal axis shows the unique numbers assigned to the OTIS's.

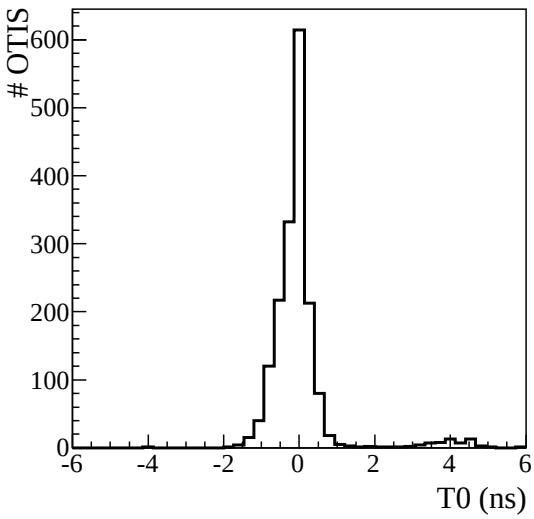

(d) Distribution of t0s after six iterations.

Figure 5.13: Results of calibration of electronic time offsets.

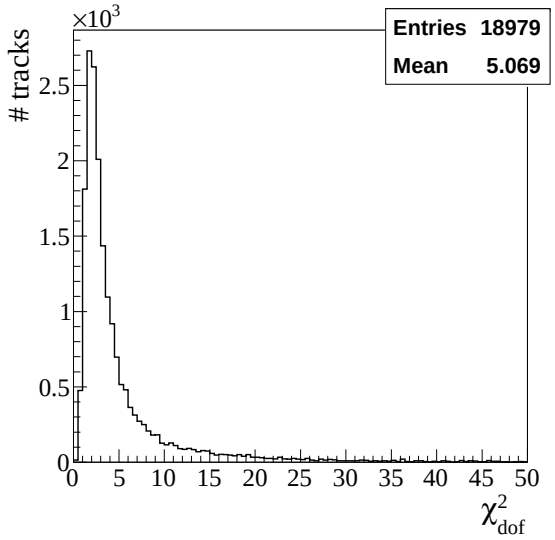

(a) χ^2_{dof}–distribution of tracks after six t_0–calibration iterations. Drift time information was used in the track fit and the event time was calculate on the fly.

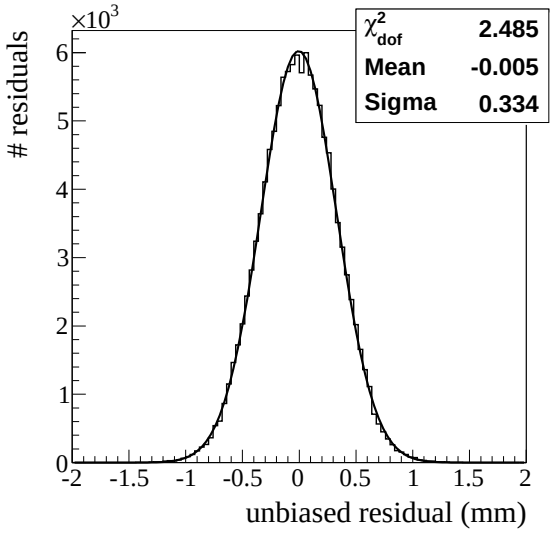

(b) Distribution of residuals for hits on track in vertical layers of the Outer Tracker after six t_0-calibration iterations. The distribution was fitted with a Gaussian.

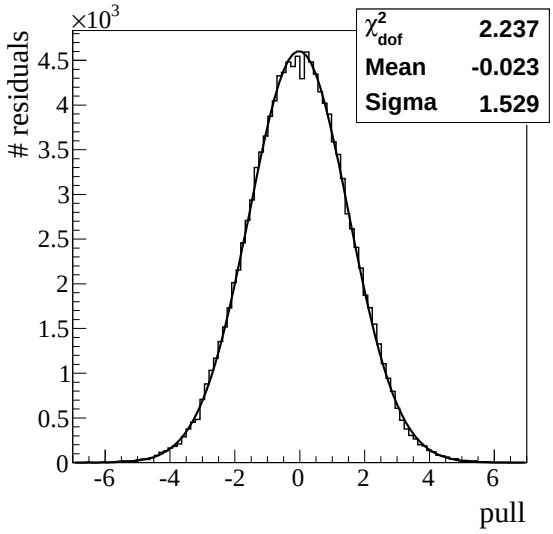

(c) Pull distribution of residuals for hits on track in vertical layers of the Outer Tracker after six t_0–calibration iterations. The distribution was fitted with a Gaussian.

Figure 5.14: Effect of the calibration of the electronic time offset on fitted tracks.

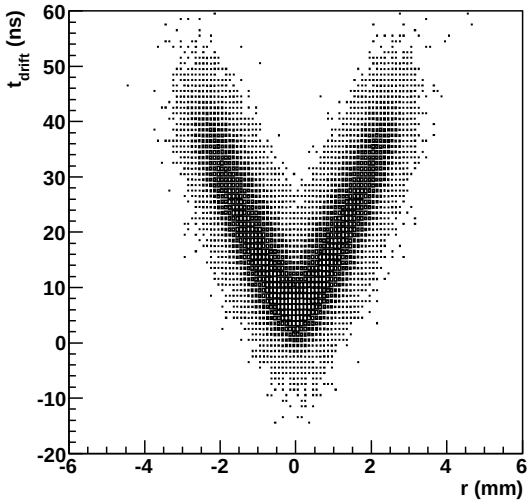

(a) Two dimensional histogram of the drift time for each hit on track plotted versus the shortest distance between the track and corresponding wire which was hit.

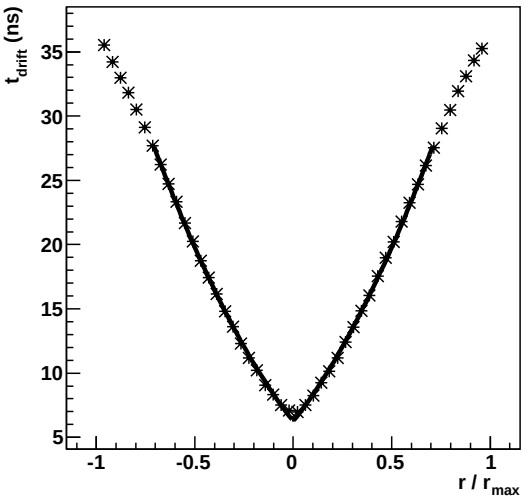

(b) Graph of the mean value of the Gaussian distributions that were fit to the projection on the vertical axis of each bin on the horizontal axis of figure (a). The width of these Gaussian is used as an error on each mean value. A second order polynomial was fitted to the graph for an appropriate range.

Figure 5.15: Illustration of the method used to obtain the $t(r)$–relation.

5.8 Calibration of the $t(r)$–Relation

Once the t_0s are known for all OTISs containing hits, an attempt is made to calibrate the $r(t)$-relation. Until now, a linear $r(t)$-relation was assumed with a constant term of 0 and a slope of 0.017 ns per µm. The $r(t)$-relation was determined to be quadratic from the data gathered during a beam test in 2005 [28]. It was the goal of this calibration procedure to test whether this relation could be recovered using cosmic muons.

5.8.1 Method

Instead of obtaining the $r(t)$–relation from the data its inverse, the $t(r)$–relation is generally preferred. The main reason for this choice is that the shape of the $t(r)$–relation is easily described by a polynomial in r, while the description of the $r(t)$–relation would be much more complex. Once the $t(r)$–relation is known, it is numerically inverted to obtain the $r(t)$–relation.

The $t(r)$-relation is expected to vary little from module to module and is obtained for the entire Outer Tracker. To obtain the $t(r)$-relation, only hits from tracks with a χ^2_{dof} less than 5 are considered. For each hit the drift time is plotted versus the unbiased distance between the track and the wire; the drift time is obtained using equation 4.8 and the track fit method is used to determine the event time. The result is plotted in figure 5.15a.

For each bin on the horizontal axis of figure 5.15a, a projection is made on the entire vertical axis and a Gaussian distribution is fit to the resulting histogram. The average value and its uncertainty of these Gaussians are shown in figure 5.15b. A second order polynomial is fitted[3]

[3]Note that the fit is performed on $|r/r_{max}|$.

to these mean values to obtain the $t(r)$-relation. The $t(r)$-relation thus obtained is then put into the reconstruction software and the entire procedure is repeated.

5.8.2 Results

The effect of the calibration of the $t(r)$-relation on the quality of the track fit is shown in figures 5.16a, 5.16b and 5.16c. They show the χ^2_{dof} distribution for all tracks, unbiased residual distribution for hits and the pull distribution for these residuals, respectively. Since the t_0s were calibrated simultaneously these figures need to be compared to the results shown in section 5.7.2.

By comparing figure 5.16a to figure 5.14a, it can be seen that the average χ^2_{dof} has improved from 4.7 to 3.4. Comparing figure 5.16c and 5.14c, the χ^2_{dof} of the Gaussian fit to the pull distribution is seen to have improved from 1.5 to 1.2.

The width of the unbiased residual distribution has, however, increased significantly from 334 to 420 microns, as can be seen by comparing figures 5.16b and 5.14b. However, as the data exceed the fit at the centre, and show large tails, the real resolution might be somwhat smaller than 420 μm.

5.8.3 Discussion

There are two problems with the method of obtaining the $t(r)$-relation described in section 5.8.1. The limits on the value of the drift radius are determined by the geometry of the straws in the OT; the drift distance can vary between 0 and 2.45 mm. Drift radii of less than 0 or more than 2.45 mm can only be the result of the resolution in the determination of the drift time; these drift radii are much less likely to occur. This can be seen in figure 5.15a as a flattening of the histogram for values of the driftradius close to 0 and 2.45 mm. When slices are fit with a Gaussian, slices close to 0 or 2.45 mm are affected. The distribution of drift times in such a slice is no longer well described by a Gaussian; the mean value of the Gaussian will be biased away from the limit. Furthermore, creating slices along an axis effectively ignores errors on the measurement of the quantity along that axis.

This problem can partially be addressed by ignoring slices that correspond to drift radii close to their limit. Slices corresponding to high drift radii have been ignored in the calibration procedure. Unfortunately, slices corresponding to small drift radii contain more information on higher order terms in the polynomial used to describe the $t(r)$-relation and should thus not be ignored. This causes a bias toward stronger higher order terms.

These problems can only be remedied by using a more complex method capable of taking into account the errors on both variables and also the cutoff of the expected values of the variables. Such methods exist, but are outside of the scope of this thesis.

At this moment, it is unclear why the calibration of the $t(r)$-relation simultaneously improves the average χ^2_{dof} of tracks, while worsening the resolution and keeping the pull distribution constant. Any more complex method of calibrating the $t(r)$-relation should show an improvement in both respects.

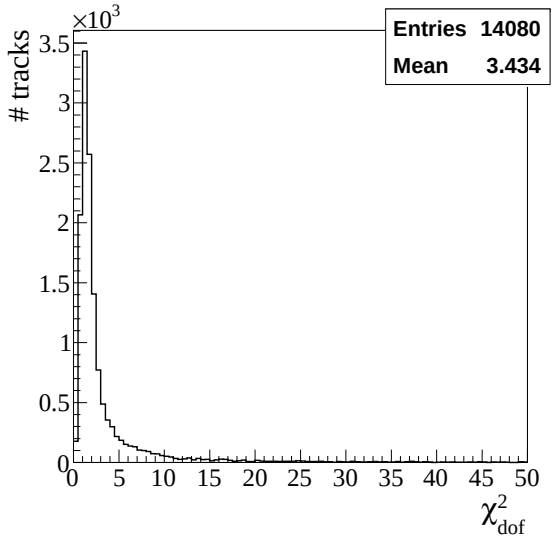

(a) χ^2_{dof}–distribution of tracks after six calibration iterations of the $t(r)$-relation.

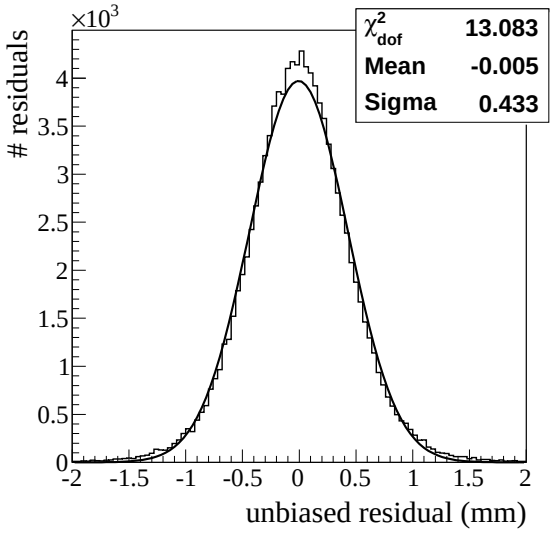

(b) Distribution of residuals for hits on track in vertical layers of the Outer Tracker after six calibration iterations of the $t(r)$-relation. The distribution was fitted with a Gaussian.

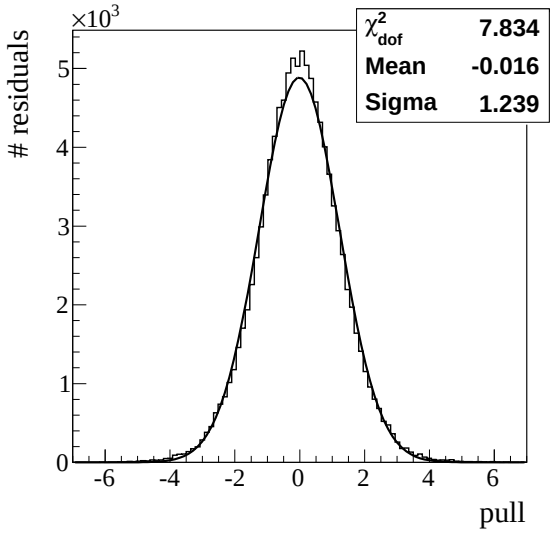

(c) Pull distribution of residuals for hits on track in vertical layers of the Outer Tracker after six calibration iterations of the $t(r)$-relation. The distribution was fitted with a Gaussian.

Figure 5.16: Results of the calibration of the $t(r)$–relation.

Chapter 6

Panoramix: The LHCb Event Display

6.1 The LHCb Software Framework

LHCb consists of multiple subdetectors and systems, which all produce data needed to study CP-violation and look for physics beyond the Standard Model. There are, however, a large number of steps to take in order to go from raw data to physics results, and all of these steps involve software. All of the LHCb software is built around a central architecture and framework named Gaudi [37].

One of the main concepts used in Gaudi is the interface. An interface defines what a part of the software should do without implementing it. Gaudi is a collection of interfaces that define all of its features. Additionally, an implemetation is provided for some interfaces that define how Gaudi is configured and run.

The use of interfaces enables code to be independent of the details of the implementation of any other code, which prevents unwanted interference between different parts of the software. It is also possible to create several implementations of an interface and choose which should be used at run time.

Gaudi extensively makes use of object oriented programming. Interfaces are represented by abstract objects, and objects that implement an interface inherit from it.

The data that is recorded after every collision in the LHC is encapsulated in objects in the software, which are described by the LHCb event model. Because access to data objects must be fast and they are only implemented in one way, interfaces are not used to describe them.

The event model together with all of the interfaces of the LHCb software provide a scientist developing code with all information needed.

6.1.1 Separation Between Data and Processing

In general object oriented programming, objects contain the methods needed to transform the data they contain. The processing of physics data, however, is better described by a clear distinction between data and processing. The decision was therefore made to completely separate objects that describe data from objects that are used to process it. This also reflects the fact that objects describing processing elements will evolve much faster than objects describing data.

6.1.2 Services, Algorithms and Tools

The main function of the LHCb software is the processing of events. This enables a clear separation of code that provides information that is the same for all events and code that needs to be executed for each event.

This is reflected in the LHCb software through a separation of code into services and algorithms: services provide information across events, whereas algorithms are executed for each event in a specific order.

A description of the geometry of the detector, the strength of the magnetic field in the detector and information about particles that might be detected are examples information provided by services. Algorithms are, for example, used to reconstruct track segments in different subdetectors and to combine these segments to form tracks; algorithms are optimised to perform a single task.

To prevent duplication, code that is not specific to one algorithms is implemented as so-called tools, which can be configured for and used by different algorithms. A tool is always defined by an interface to perform a single task.

6.1.3 Run-time Phases

The separation of code into services and algorithms is also present at run-time. The execution of a program based on Gaudi is strictly ordered in several phases: configuration, initialisation, execution of algorithms for all events and finalisation. At the end of each phase, checks are done to make sure that the program is ready to enter the next phase.

During the configuration phase, the configuration of algorithms and services for a specific task is read from files supplied by the user. They contain information on which algorithms need to be executed, values of all parameters needed by services and algorithms and the order in which selected algorithms are to be executed.

The next phase is the initialisation; during this phase, the configuration that was loaded is applied to algorithms and services. An important part of this phase is the start up of the services that provide input and output of data to the program.

The initialisation phase is followed by the execution phase, during which events are read from input and algorithms are executed for each event. Any output generated during this phase can be stored.

The execution phase is followed by the finalisation phase, during which any calculations that require data from all events are done. At the end of the finalisation phase, all open input and output connections are closed.

6.1.4 Transient Stores

In the LHCb software, code can only be accessed through the interface that defines its function. Because algorithms are optimised to perform a single task, many algorithms are executed for each event. To allow data to flow between algorithms, without the need for dependencies in the code, the transient event store (TES) has been implemented.

The transient event store is unique at run-time and algorithms are able to access it through a service. All objects described by the event model can be stored in, retrieved from and updated

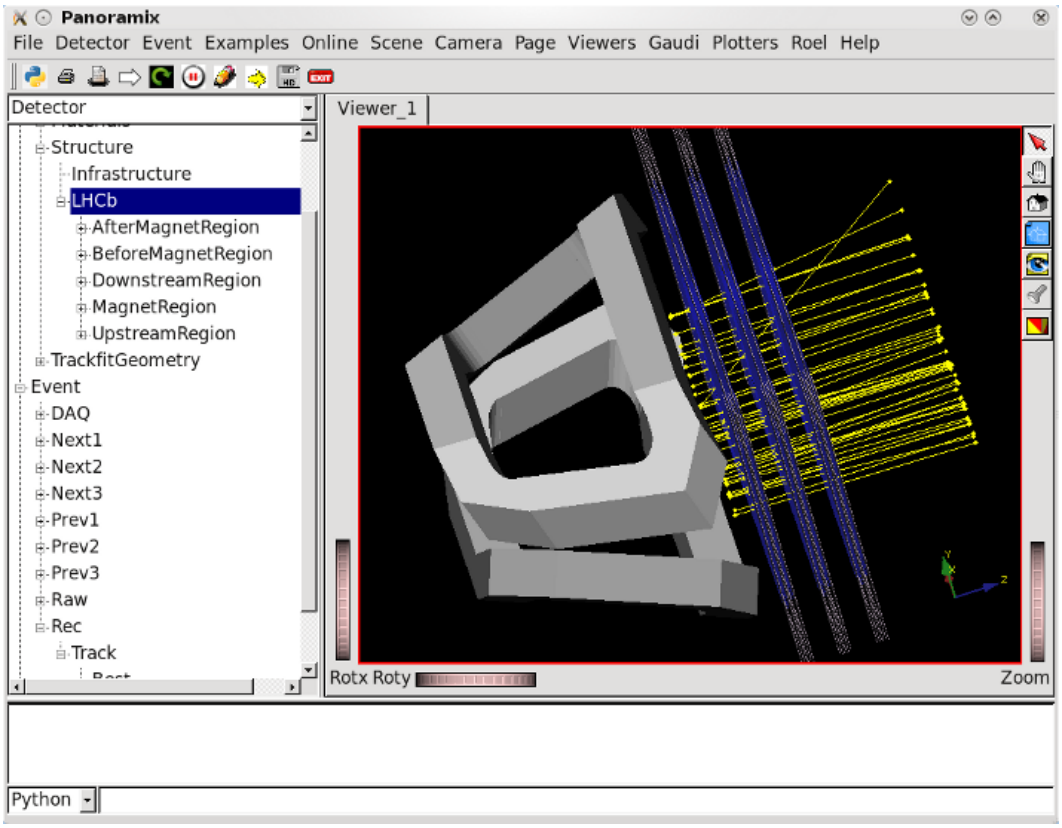

Figure 6.1: An overview of the main Panoramix window. The top part is reserved for a menu bar and toolbar. The centre part consists of a tree view of all transient stores to the left and an area reserved for 3D visualisation to the right. The bottom part of the GUI can be used to enter commands and display text output.

in the TES by all algorithms. The store is reset before a new event is read from disk and before any algorithms are executed for the new event.

The TES uses a tree-like topology to store data, and data can be accessed using a slash separated path that describes a location on the tree. The raw hits from the Outer Tracker are, for example, by default stored in the TES at: /Event/Raw/OT/Times.

Apart from event data, algorithms can also access geometrical information about the detector using a service. This information is stored in the transient detector store and remains over the course of a job.

Algorithms might also produce histograms, which are stored in the transient histogram store and accessible through the histogramming service.

6.1.5 Visualisation Using Panoramix

It is often desirable to be able to graphically display event data. This allows data to be shown with a high density and gives an intuitive overview of an event. This is useful in tasks like debugging of an analisys, online monitoring of events, visualisation of the detector geometry or generation of images. The application providing this functionality within the LHCb software is called Panoramix. Panoramix' graphical user interface (GUI) is designed to serve several purposes. Its main goal is to allow the user to select which objects are visualised. The nature of

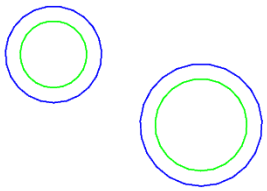

Figure 6.2: A double hit in the Outer Tracker. The circles correspond to a drift time assuming either minimal or maximal drift time.

the transient event store requires this to be done on a per event basis, so the GUI also contains elements that allow the user to go through the data event by event.

As within the LHCb software framework all data is stored in transient stores, the main component of the GUI through which objects can be selected is a tree view of all stores. Figure 6.1 shows an overview of Panoramix' main window. A fully three-dimensional approach to the visualisation of objects was taken, and two-dimensional projections can be created, too.

6.2 Visualisation of Outer Tracker Drift Times

Raw data from the outer tracker is visualised in Panoramix by a line at the position of the wire in the straw that was hit. This is done because until a track has been reconstructed, the y-position of a hit and its associated signal propagation time, are unknown.

The maximum and minimum signal propagation times are, however, known, and the corresponding range of possible drift times can be calculated. By adding to the code that visualises raw data from the Outer Tracker, a raw drift time can now be visualised by two circles with radii that correspond to a drift time assuming the maximum or minimum signal propagation time, respectively. An example of this visualisation is shown in figure 6.2. This view only works as intended when the direction of viewing is exactly parallel to the wire that was hit.

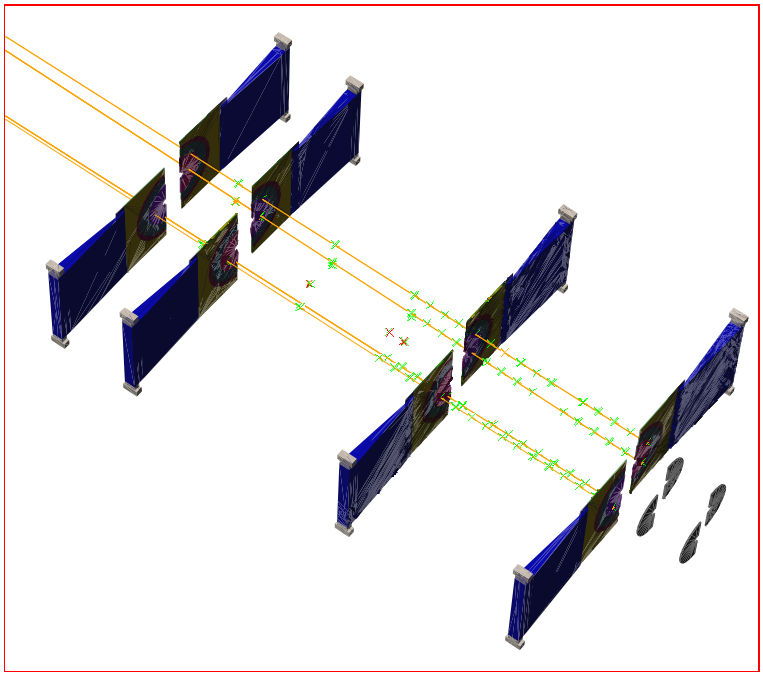

Figure 6.3: An isomeric view of the VELO showing several sensors; reconstructed tracks with their associated hits are also shown.

6.3 Visualisation of Other Events

6.3.1 Tracks in the VELO During Lhcb Injection Tests

During injection tests into the LHC from the SPS, the SPS beam is stopped by a large amount of material contained in a beam stopper called TED which can be positioned in the path of the beam just before it enters the LHC. The position of this TED is such that particles travel toward the LHCb detector, entering it from the downstream side. The Scintillating Pad Detector (SPD) calorimeter was set up as a multiplicity trigger for these splashes of particles, and depending on the expected amount of particles, subdetectors were turned on or off.

During the measurements of cosmic rays in LHCb, triggers occurred with a frequency of about 10Hz. This is the combined rate of forward and backward going cosmics, this means that the rate of cosmics travelling in the direction of the VELO is 5Hz. If a uniform angular distribution is assumed, this leads to a flux of $8.0 * 10^{-3} \mathrm{m}^{-2}\mathrm{s}^{-1}\mathrm{sr}^{-1}$. The angular acceptance for the VELO is 300 mrad and the radius of its sensors 48 mm. Using these, the rate of cosmics, triggered by the calorimeter, in the VELO can be estimated to be $1.6 * 10^{-5}\mathrm{s}^{-1}$. In reality this rate will be significantly smaller, because the assumption of isotropically distributed directions of cosmics is not valid; cosmics favour vertical directions due to a larger amount of absorbing material along horizontal paths.

The estimated rate of cosmics is so low that any measurement would not result in a significant amount of cosmics being detected by the VELO. The density and direction of particles travelling through the VELO during the LHC injection tests is such that up to 10 particles are expected to traverse the VELO simultaneously. An example of an image of these particles in the VELO is shown in figure 6.3.

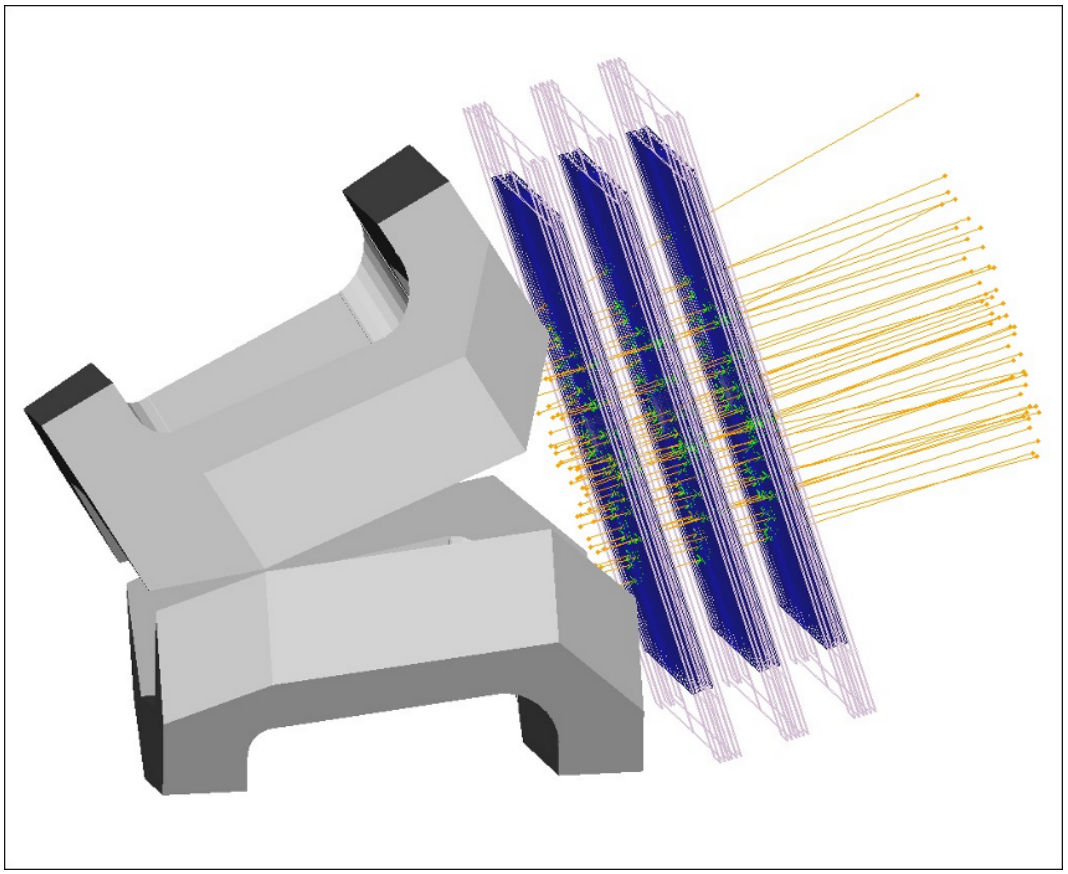

Figure 6.4: An isomeric view of Outer Tracker and the magnet; reconstructed tracks and their associated hits are also shown.

6.3.2 Tracks in the Outer Tracker During the LHC Startup

During the LHC startup in September of 2008, The SPD calorimeter was set up as a multiplicity trigger; the Outer Tracker was turned on and data was recorded. The events recorded included a few beam-gas interactions and splashes of particles from the bunches that were stopped by an LHC collimator in its closed position. An example of such an event is shown if figure 6.4.

Chapter 7

Conclusions and Outlook

7.1 Conclusions

Cosmic muon data recorded with the LHCb detector in November and December of 2008 has been analysed as part of the commissioning of the LHCb Outer Tracker. Looking at the results of this analysis, several conclusions can be drawn.

The frequency with which straws in the Outer Tracker give a signal shows that the majority of the straws fires in 0.05 % of the events or less, which implies that the amount of noise in the Outer Tracker is low. If drift time information is not used in the reconstruction of tracks from cosmic muons, the resolution of reconstruction of Outer Tracker tracks is 1.41 mm. Approximately twenty thousand tracks are reconstructed, indicating that the Outer Tracker and the reconstruction software function well.

To be able to use drift time information in the reconstruction of tracks from cosmic muons, the event time must be known. Four methods to obtain the event time have been tested. Using the asymmetry of the amount of signal collected by the LHCb calorimeter in two consecutive readout windows gives the event time with a resolution of at most 2.6 ns. Only tracks from muons that arrive close to the end of a readout window can be successfully reconstructed with this method, which yields an average χ^2_{dof} of 6.40 and a resolution of 341 μm.

The drift times themselves can also be used to obtain t_{ev}. The average drift time gives the event time with a resolution of at most 3.0 ns and yields an average χ^2_{dof} of 8.15 and a resolution of 354 μm. Correcting the event time obtained from the average drift time with the average drift time residuals from double hits improves the average χ^2_{dof} to 5.75 and the resolution to 332 μm. Both of these methods are unable to correctly take the error on drift times into account. Using the track fit to determine the event time ensures that errors are automatically treated correctly and yields the event time with a resolution of at most 2.6 ns. Using this method, the average χ^2_{dof} improves to 4.8 and the resolution becomes 344 µm.

The event times given by the calorimeter software are shown to systematically differ from the event times obtained using drift times. This might be due to the calibration of the method being based on a Monte-Carlo simulation that is not consistent with reality. The methods using drift times are shown to yield event times with a difference of at most 1 ns.

Once the event time is under control, it is possible to extract calibration information from cosmic muons. The electronic time offsets per OTIS are determined, and use of their updated values improves the resolution to 334 µm. An attempt was also made to obtain the $r(t)$–relation, but its use did not improve the quality of reconstructed tracks.

7.2 Outlook

Since the $r(t)$–relation could not be extracted, more work is needed to extract it from cosmic muon data. It will be easier to obtain $r(t)$–relation from collision data and the with restart of the LHC collisions look to be available soon. Appendix A briefly discusses the first collisions in the LHCb detector, which occured on the 23rd of November 2009.

So far, alignment has only been done using tracks reconstructed without the use of drift time information. The accuracy of alignment information will improve if drift times are used, either using data from collisions or cosmic muons.

Bibliography

[1] A.D. Sakharov, *Violation of CP Invariance, C Asymmetry, and Baryon Asymmetry in the Universe*, Pisma Zh. Eksp. Teor. Fiz. **5** (1967) 32.

[2] M. Kobayashi and T. Maskawa, *CP-Violation in the Renormalizable Theory of Weak Interaction*, Prog. Th. Phys. **49** (1973) 652.

[3] LHCb Collaboration, A. Augusto Alves *et al.*, *The LHCb Detector at the LHC*, JINST **3** (2008) S08005.

[4] N. Cabibbo, *Unitary Symmetry and Leptonic Decays*, Phys. Rev. Lett. **10**(12) (1963) 531.

[5] S. L. Glashow, J. Iliopoulos, and L. Maiani, *Weak Interactions with Lepton-Hadron Symmetry*, Phys. Rev. D **2**(7) (1970) 1285.

[6] J.H. Christenson, J.W. Cronin, V.L. Fitch, and R. Turlay, *Evidence for the 2 π decay of the K_0^2 meson*, Phys. Rev. Lett. **13** (1964) 138.

[7] R. Aleksan, B. Kayser, and D. London, *Determining the Quark Mixing Matrix from CP-violating Asymmetries*, Phys. Rev. Lett. **73**(1) (1994) 18.

[8] *BABAR* Collaboration, B. Aubert *et al.*, *Measurement of the CP Asymmetry Amplitude $sin2\beta$ with B Mesons*, Phys. Rev. Lett. **89**(20) (2002) 201802.

[9] Belle Collaboration, A. Abashian *et al.*, *Measurement of the CP Violation Parameter $\sin 2\phi_1$ in B_d^0 Meson Decays*, Phys. Rev. Lett. **86**(12) (2001) 2509.

[10] L. E. Piilonen, *Measurements of V_{ub} and mixing by Belle and BABAR*, Nucl. Phys. B Proc. Suppl. **115** (2003) 227.

[11] D0 Collaboration, J. Ellison, *Measurement of B_s Oscillations and CP Violation Results from D0*, Nucl. Phys. A **827**(1-4) (2009) 475c.

[12] CDF Collaboration, A. Abulencia *et al.*, *Measurement of the B_s–$\overline{B}_s$ Oscillation Frequency*, Phys. Rev. Lett. **97**(6) (2006) 062003.

[13] E. T. Worcester, *The Final Measurement of Epsilon'/Epsilon from KTeV*, ArXiv e-prints (2009) .

[14] O. Deschamps, *CKM global fit and constraints on New Physics in the B meson mixing*, 0810.3139, 2008.

[15] Particle Data Group Collaboration, C. Amsler *et al.*, *Review of particle physics*, Phys. Lett. **B667** (2008) 1.

[16] R. Aleksan, I. Dunietz, and B. Kayser, *Determining the CP-violating phase γ*, Z. Phys. C **54** (1992) 653.

[17] A. Dedes, H. K. Dreiner, and U. Nierste, *Correlation of $B_s \to \mu^+\mu-$ and $(g-2)_\mu$ in Minimal Supergravity*, Phys. Rev. Lett. **87**(25) (2001) 251804.

[18] Blanke, M. and Buras, A. J. and Guadagnoli, D. and Tarantino, C., *Minimal flavour violation waiting for precise measurements of ΔM_s, $S_{\psi\phi}$, A^sSL, $|V_{ub}|$, γ and $B^0_{s,d} \to \mu^+\mu^-$*, J. High Ener. Phys. **2006**(10) (2006) 003.

[19] CDF Collaboration, T. Aaltonen *et al.*, *Search for $B_s \to \mu^+\mu^-$ and $B^0_d \to \mu^+\mu^-$ decays with $2fb^{-1}$ of $p\bar{p}$ collisions*, Phys. Rev. Lett. **100** (2008) 101802.

[20] Rai Choudhury, S. and Gaur, N., *Dileptonic decay of B_s mesons in SUSY models with large* $\tan\beta$, Phys. Lett. B **451** (1999) 86.

[21] D. Martinez, J.A. Hernando, and F. Teubert, *LHCb potential to measure/exclude the branching ratio of the decay $B_s \to \mu^+\mu^-$*, LHCb-2007-033, 2007.

[22] H Ruiz, *The LHCb trigger: algorithms and performance*, 2009.

[23] M Needham, *Performance of the LHCb Track Reconstruction Software.*, CERN-LHCb-2007-144, 2008.

[24] LHCb Collaboration, S. Amato *et al.*, *LHCb Magnet: Technical Design Report*, CERN-LHCC/2000-007, 1999.

[25] LHCb Collaboration, A. Jr. Augusto Alves *et al.*, *The LHCb Detector at the LHC*, Jinst. **3**(8) (2008) 15.

[26] V Gromov and T Sluijk, *Electrical properties of various types of straw tubes considered for the LHCb outer tracker*, CERN-LHCb-2001-001, 2001.

[27] M. Blom, private communication, 2009.

[28] G. W. van Apeldoorn *et al.*, *Beam Tests of Final Modules and Electronics of the LHCb Outer Tracker in 2005*, CERN-LHCb-2005-076, 2005.

[29] LHCb Collaboration, P. Barbosa-Marinho *et al.*, *LHCb Outer Tracker: Technical Design Report*, CERN-LHCC/2001-024, 2001.

[30] E Bos and M Merk, *Reconstruction of charged particles int he LhCb experiment.*, Ph.D. thesis, Vrije Univ. Amsterdam, Amsterdam, 2009.

[31] J Van Tilburg and M Merk, *Track simulation and reconstruction in LHCb.*, Ph.D. thesis, Vrije Univ. Amsterdam, Amsterdam, 2005.

[32] M. Needham, private communication, 2009.

[33] C Grupen, *Astroparticle Physics*, Springer-Verlag Berlin, 2005.

[34] P. H. Barrett, L. M. Bollinger, G. Cocconi, Y. Eisenberg, and K. Greisen, *Interpretation of Cosmic-Ray Measurements Far Underground*, Phys. Rev. Lett. **24**(3) (1952) 133.

[35] J. Amoraal, private communication, 2009.

[36] Y. S. Amhis and M-H. Schune, *Time alignment of the electromagnetic and hadronic calorimeters, reconstruction of the* $B \to D^-\rho(770)^+, B_s \to D_s^-\rho(770)^+$ *and* $B_s \to D_s^- K^{*+}(892)$ *decay channels with the LHCb detector.*, Ph.D. thesis, Paris, Universite de Paris XI Orsay, Paris, 2009.

[37] G. Barrand, I. Belyaev, *et al.*, *GAUDI – A software architecture and framework for building HEP data processing applications*, Comp. Phys. Comm. **140**(1 - 2) (2001) 45.

[38] R Brun and F Rademakers, *ROOT - An Object Oriented Data Analysis Framework*, volume A 389 of *Nucl. Inst. & Meth. in Phys. Res.*, pages 81–86. Proceedings at AIHENP'96 workshop, Lausanne, 1996.

Student's Contributions

The following is an overview of the work done during the research project of which this thesis is the result. Work done during the Cern summer school of 2007 is described in the next section.

7.3 Research Project

During the research project, the author has:

- Spent 12 weeks at a summer school at Cern working on several widgets for the graphical user interface of the ROOT [38] analysis framework.
- Modified the LHCb event display software to enable visualisation of Outer Tracker hits without needing to first reconstruct tracks.
- Presented preliminary results on the timing of the Outer Tracker when measuring cosmic muons to the LHCb commissioning meeting.
- Developed software to obtain the event time of cosmic muon events in the following ways:
  - Using information provided by the calorimeter software.
  - Using the average drift time of Outer Tracker hits.
  - Using the average drift time of Outer Tracker hits, corrected using drift time residuals from all hits or double hits.
  - Using the track fit software.
- Created a minimal configuration of the LHCb reconstruction software that enables the reconstruction of cosmic muons.
- Prepared computing hardware and network infrastructure for use during the analysis workshop of the Nuked LHCb group.
- Developed software to extract, store and apply Outer Tracker calibration constants using cosmic muon data. Calibration constants are extracted from data using dedicated software and stored in a plain text file. The plain text file is read during the initialisation of the LHCb reconstruction software and stored calibration constants are applied.
- Developed software to store the output of the LHCb reconstruction software in a series of sequentially named files.

Figure 7.1: An example of a split button in the graphical user interface of the ROOT analysis framework.

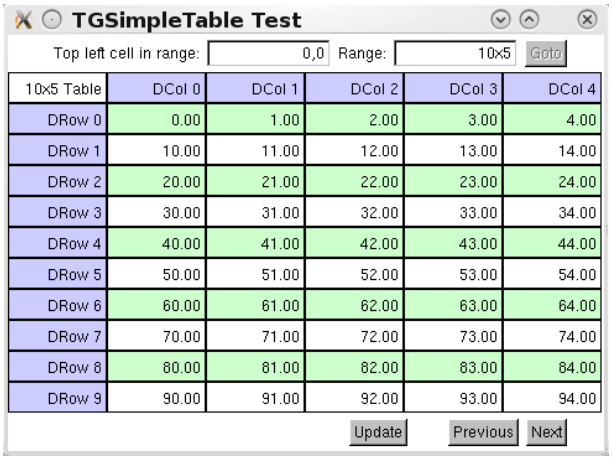

10x5 Table	DCol 0	DCol 1	DCol 2	DCol 3	DCol 4
DRow 0	0.00	1.00	2.00	3.00	4.00
DRow 1	10.00	11.00	12.00	13.00	14.00
DRow 2	20.00	21.00	22.00	23.00	24.00
DRow 3	30.00	31.00	32.00	33.00	34.00
DRow 4	40.00	41.00	42.00	43.00	44.00
DRow 5	50.00	51.00	52.00	53.00	54.00
DRow 6	60.00	61.00	62.00	63.00	64.00
DRow 7	70.00	71.00	72.00	73.00	74.00
DRow 8	80.00	81.00	82.00	83.00	84.00
DRow 9	90.00	91.00	92.00	93.00	94.00

Figure 7.2: An example of a table widget in the graphical user interface of the ROOT analysis framework.

7.4 Summer School

From June 10th until September 2nd 2007 I attended the Cern summer school. During these 12 weeks I worked in the PH department under the supervision of Ilka Antcheva on several widgets for the graphical user interface of the ROOT analysis framework. I developed a new type of split button, of which an example is shown in figure 7.1. Once that had been completed, I spent the remainder of my time at Cern developing a table widget. The table widget can be used to visualise data as a table; data stored in different formats can be visualised. Figure 7.2 shows an example of the widget.

Samenvatting

Het LHCb experiment op Cern onderzoekt het verval van B mesonen. De doelen van het onderzoek zijn de zoektocht naar fysica die verder gaat dan het Standaard Model van elementaire deeltjes en het testen van beschrijving van CP schending in het Standaard. De Outer Tracker is een belangrijk onderdeel van de LHCb detector en heeft tot doel het meten van de banen van geladen deeltjes. Om te testen of de Outer Tracker correct functioneert zijn over een periode van enkele uren kosmische muonen gemeten.

Ik heb deze data geanalyseerd en de resultaten van die analyse zijn beschreven in deze scriptie. Er zijn enkele belangrijke verschillen tussen het meten van kosmische muonen en deeltjes afkomstig van botsingen. Het belangrijkste verschil is dat de aankomsttijd van kosmische muonen niet bekend is. Ik heb vier methoden onderzocht om deze aankomsttijd te bepalen. Met behulp van de beste methode om de aankomsttijd van muonen te bepalen kunnen hun sporen met een nauwkeurigheid van 334 μm worden gereconstrueerd. Ook is het mogelijk gebleken om de elektronica die de detector uitleest te ijken met behulp van de geanalyseerde data.

Appendix A

First Collisions

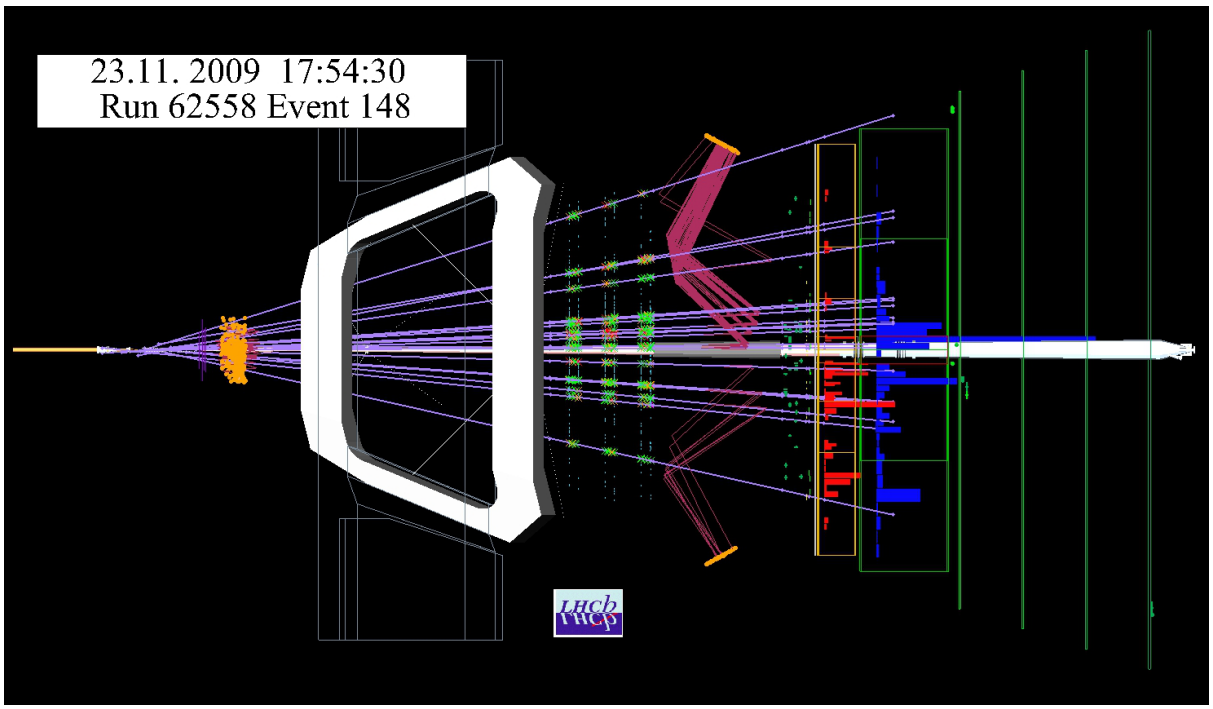

Figure A.1: An event display of one of the first proton–proton collisions recorded with the LHCb detector.

On the 23rd of November 2009, protons collided for the first time in the Large Hadron Collider. The center of mass energy was 900 GeV and all four experiments recorded collisions. Figure A.1 shows an event display of one of the first proton collisions recorded with the LHCb detector. The first collisions mark the start of a long period of gathering data and extracting physics from that data. It is an exciting time.